

WATER MASERS IN THE ANDROMEDA GALAXY: II. WHERE DO MASERS ARISE?

NIKTA AMIRI¹ & JEREMY DARLING

Center for Astrophysics and Space Astronomy, Department of Astrophysical and Planetary Sciences, University of Colorado, Boulder, CO, 80309-0389, USA

ABSTRACT

We present a comparative multi-wavelength analysis of water maser-emitting regions and non-maser-emitting luminous 24 μm star-forming regions in the Andromeda Galaxy (M31) to identify the sites most likely to produce luminous water masers useful for astrometry and proper motion studies. Included in the analysis are Spitzer 24 μm photometry, Herschel 70 and 160 μm photometry, H α emission, dust temperature, and star formation rate. We find significant differences between the maser-emitting and non-maser-emitting regions: water maser-emitting regions tend to be more IR-luminous and show higher star formation rates. The five water masers in M31 are consistent with being analogs of water masers in Galactic star-forming regions and represent the high-luminosity tail of a larger (and as yet undetected) population. Most regions likely to produce water masers bright enough for proper motion measurements using current facilities have already been surveyed, but we suggest three ways to detect additional water masers in M31: (1) Re-observe the most luminous mid- or far-IR sources with higher sensitivity than was used in the Green Bank Telescope survey; (2) Observe early-stage star-forming regions selected by mm continuum that have not already been selected by their 24 μm emission, and (3) Re-observe the most luminous mid- or far-IR sources, and rely on maser variability for new detections.

Keywords: galaxies: individual (M31) — galaxies: ISM — galaxies: star formation — Local Group — masers — radio lines: galaxies

1. INTRODUCTION

Water masers can arise in star-forming regions, in shocks, in stellar atmospheres, and in the vicinity of massive black holes (see reviews by Reid & Moran 1981; Elitzur 1992; Lo 2005). They can indicate specific physical conditions and provide high brightness temperature sources for precise astrometry and proper motion studies (see review by Reid & Honma 2014). While water masers' presence and intensity cannot be predicted based on observed conditions in any given physical setting (mostly due to nonlinear amplification of small-scale conditions and anisotropic emission), there is good observational evidence indicating where water masers are most likely to be observed. In the Galaxy, for example, the water maser detection rate toward (ultra)compact H II regions is typically 50% or higher (e.g., Churchwell et al. 1990; Urquhart et al. 2011).

The utility of water masers for extragalactic proper motion studies has been demonstrated in the Lo-

cal Group and in water maser disks associated with massive black holes (e.g., Brunthaler et al. 2005; Humphreys et al. 2013). In the Local Group, the masers are associated with star formation and can be used to measure systemic proper motions and proper rotation (also known as “rotational parallax”). This has been done for M33 and IC 10 (Brunthaler et al. 2005, 2007), but detected water masers were notably absent from the Andromeda Galaxy (M31) until recently (Sullivan 1973; Greenhill et al. 1995; Imai et al. 2001; Darling 2011). The proper motion of M31 is a key quantity for Local Group dynamics (e.g., Loeb et al. 2005), and while Sohn et al. (2012) and van der Marel et al. (2012) obtained a constraint on the tangential velocity M31 of $\leq 34.3 \text{ km s}^{-1}$ (1σ) using the *Hubble Space Telescope*, suggesting a nearly radial Milky Way-Andromeda trajectory, a second completely independent and possibly more precise measurement is worthwhile (Darling 2011; Darling et al. 2016).

Water masers in M31 have been difficult to find, in large part due to the low distance-dimmed flux density and due to the large areal size of the molecular disk: the disk is too large in angular size and the masers are too faint to simply map the entire disk in a rea-

¹Current address: Jet Propulsion Laboratory, M/S 238-600, 4800 Oak Grove Dr., Pasadena, CA 91109, USA; nikta.amiri@jpl.nasa.gov

sonable amount of observing time using current facilities. A Green Bank Telescope (GBT) ¹ survey of 506 22 μm -selected regions detected only five water masers (Darling et al. 2016). The selection method is inefficient, and the survey is barely sensitive enough to detect the most luminous Galactic analog water masers associated with star formation. Given what we know about the star-forming regions in M31 in a pan-spectral sense, we can (1) learn more about how and where luminous water masers arise, and (2) apply this knowledge to identify additional likely sites of water maser emission in M31, improving detection statistics and making future surveys more efficient. Water masers can show significant peculiar motion and variability, so the detection of additional water masers would substantially improve proper motion and rotation measurements of M31 and reduce systematic effects. An enhanced astrometric network of water masers could enable the detection of the apparent expansion of — and thus the measurement of a geometric distance to — M31 as it approaches the observer at -300 km s^{-1} (Darling 2011, 2013).

In this paper, we present a comparative multi-wavelength analysis of 22 GHz water maser-emitting and non-maser-emitting 24 μm -luminous star-forming regions in M31. We use *WISE*, *Spitzer*, and *Herschel*² infrared continuum maps, maps of derived quantities such as star formation and dust temperature, and archival catalogs to examine the differences between maser-emitting and non-maser-emitting regions, to examine correlations between observable quantities among each population, and to constrain the parameter space most likely to produce detectable water masers. Section 2 summarizes the GBT survey presented in detail in Darling et al. (2016), Section 3 describes data sources and new measurements, Section 4 refines the sample used in the analysis, Section 5 presents the results of the measurements and data collation, Section 6 examines trends and differences among the masers and non-masing regions, and Section 7 discusses the best approach to identifying new water masers in M31. Section 8 highlights the main findings of this study.

Throughout the manuscript, we assume a distance to M31 of 780 kpc when calculating luminosities from continuum or line flux measurements.

2. THE GREEN BANK WATER MASER SURVEY OF M31

¹ The National Radio Astronomy Observatory is a facility of the National Science Foundation operated under cooperative agreement by Associated Universities, Inc.

² Herschel is an ESA space observatory with science instruments provided by European-led Principal Investigator consortia and with important participation from NASA.

The water maser candidate selection for the Green Bank Telescope (GBT) survey for water masers in M31, the observing methods, data reduction, and results are presented in Darling (2011) and Darling et al. (2016). In summary, we selected bright point sources from the Spitzer 24 μm map of M31 (Gordon et al. 2006), and constructed a catalog of 506 objects from the brightest down to a point where most of the 24 μm emission becomes extended at about 4 MJy sr^{-1} (Figure 1, top). The compact 24 μm sources in M31 are likely associated with star-forming regions; strong water masers are known to arise in H II regions in the Galaxy (e.g. Walker et al. 1982), and H₂O maser luminosity correlates with far-infrared (FIR) luminosity in Galactic star-forming regions as well as in star-forming galaxies (Felli et al. 1992; Castangia et al. 2008).

We observed the 6₁₆ – 5₂₃ 22.23508 GHz ortho-water maser line toward the 506 24 μm -selected regions in late 2010, late 2011, and early 2012 (Darling 2011; Darling et al. 2016). Spectra were smoothed to 3.3 km s^{-1} channels, reaching an rms noise of ~ 3 mJy in individual spectra and 0.17 mJy in a spectral mean stack of 299 objects aligned to the CO velocity (Nielen et al. 2006). Five water masers were detected (Darling 2011), and the detection rate after removing planetary nebulae and giant stars from the sample was 1.1(0.5)% (see Section 4.1 and Darling et al. 2016). The full details of the results of water maser observations, including the results of NH₃ (1,1), NH₃ (2,2), and H66 α observations, are presented in Darling et al. (2016). In this paper, we use multi-wavelength data to investigate the physical and observed properties of water maser-emitting regions and to compare them to non-maser-emitting regions to understand where the water masers arise and how to detect additional water masers in M31.

3. MULTI-WAVELENGTH PHOTOMETRY AND DERIVED PROPERTIES

3.1. Data Sources

Table 1 summarizes the archival data used in the M31 water maser study, split into sources of photometry (H α , mid- and far-IR) and derived quantities (dust temperature and star formation rate [SFR]). Figure 1 shows 24 μm , 70 μm , 160 μm , and star formation rate maps of M31, and Figure 2 shows the dust temperature map (Smith et al. 2012). Both figures show the water masers and the non-detection locations.

Spitzer observations of M31 at 24 μm were performed using the Multiband Imaging Photometer (MIPS) instrument with Point Spread Function (PSF) of 6'' (Gordon et al. 2006). The map covers an area of approximately $1^\circ \times 3^\circ$ oriented along the major axis of M31. The MIPS data analysis tool version 2.9 (Gordon et al.

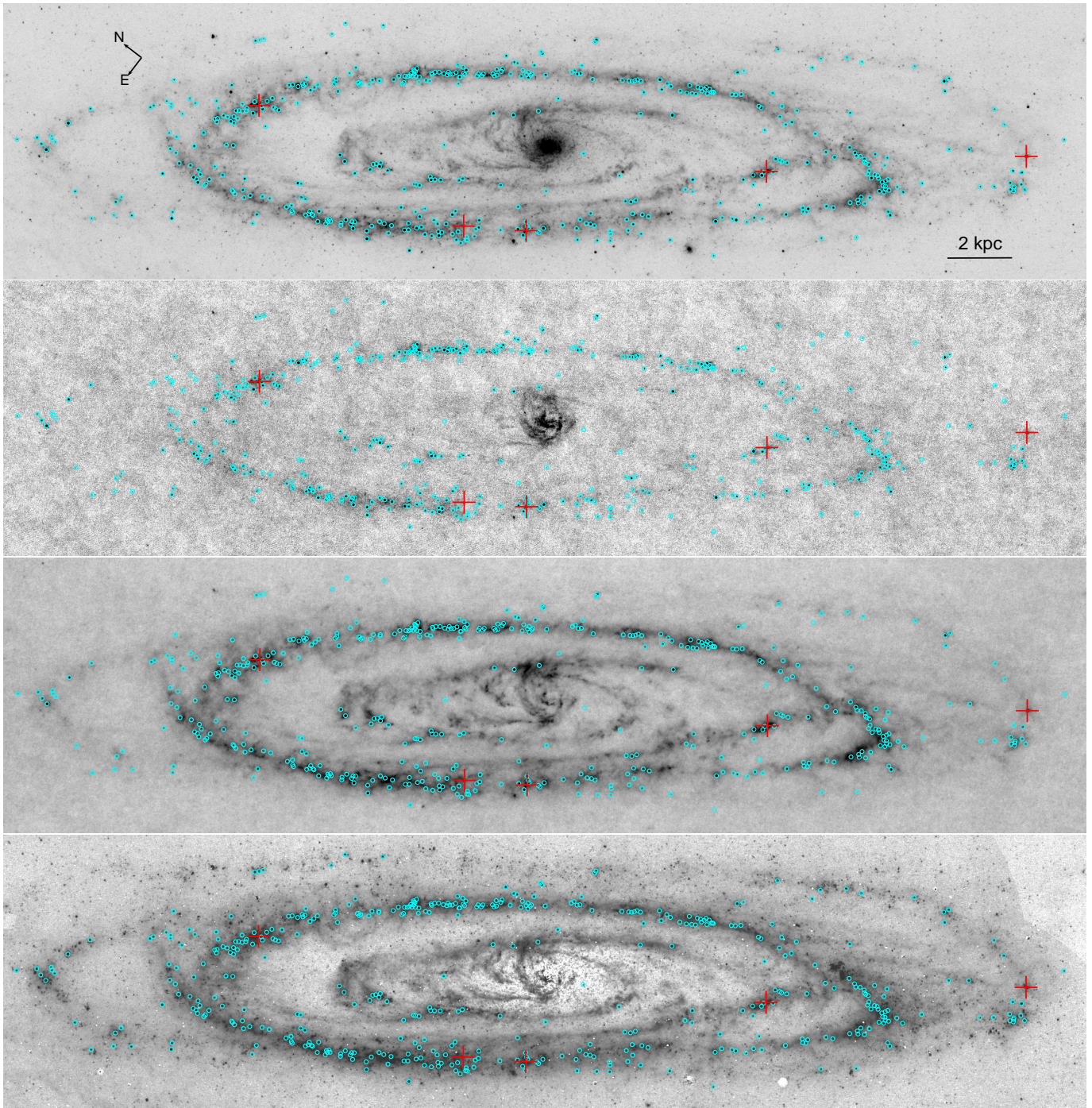


Figure 1. Infrared and star formation maps of M31. Top to Bottom: Spitzer $24\ \mu\text{m}$ (Gordon et al. 2006), Herschel $70\ \mu\text{m}$, Herschel $160\ \mu\text{m}$ (Bruno Altieri, priv. comm.), and star formation rate (Ford et al. 2013). Cyan circles show the 457 star-forming regions observed with the GBT (Darling et al. 2016). The circles are to scale, showing the $33''$ ($125\ \text{pc}$) FWHM beam. Red crosses indicate the location of the five detected water masers in M31 (Darling 2011).

Table 1. M31 Multi-Wavelength Data Sources

Data	Resolution (")	Telescope	Reference
H α	0.9–1.4	Mayall Telescope	Azimlu et al. (2011)
3.4 μm	6.1	<i>WISE</i>	Wright et al. (2010)
22 μm	22	<i>WISE</i>	Wright et al. (2010)
24 μm	6	<i>Spitzer</i>	Gordon et al. (2006)
70 μm	5.6	<i>Herschel</i>	Groves et al. (2012) ; B. Altieri (priv. comm.)
160 μm	11.4	<i>Herschel</i>	Groves et al. (2012) ; B. Altieri (priv. comm.)
T _{dust}	36	<i>Herschel</i> and <i>Spitzer</i>	Smith et al. (2012)
SFR	6	<i>Galex</i> and <i>Spitzer</i>	Ford et al. (2013)

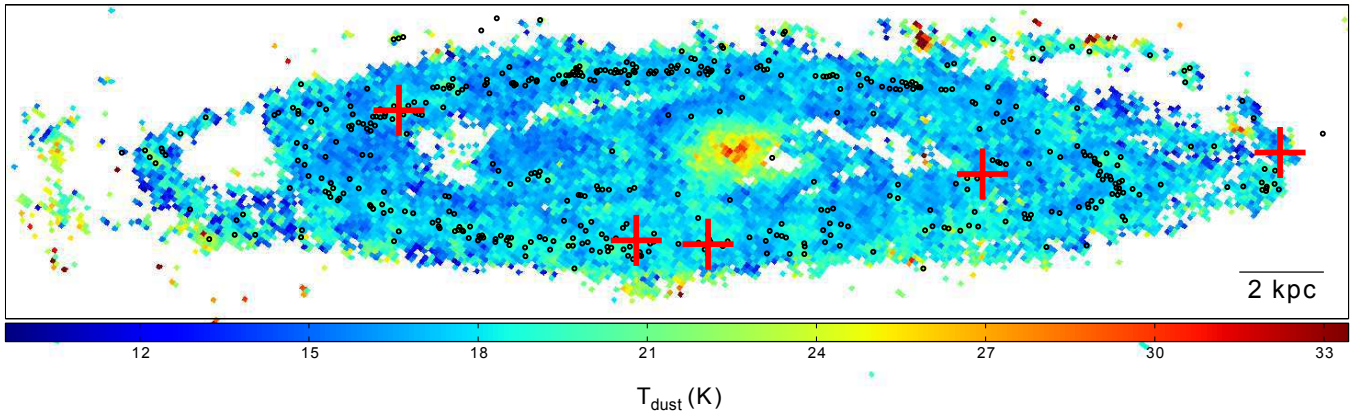


Figure 2. Dust temperature map of M31 ([Smith et al. 2012](#)). Black circles show the 457 star-forming regions observed with the GBT ([Darling et al. 2016](#)). The circles are to scale, showing the $33''$ (125 pc) FWHM beam. Red crosses indicate the location of the five detected water masers in M31 ([Darling 2011](#)).

2005) was used to produce the final mosaic map at $24\ \mu\text{m}$.

We obtained the Herschel maps of M31 at $70\ \mu\text{m}$ and $160\ \mu\text{m}$ from the public data of the Herschel archive (Pilbratt et al. 2010; Poglitsch et al. 2010). The maps were re-processed by Bruno Altieri (ESA; private communication) with unimap map-maker (Piazzo 2013). The observations were performed using the Photodetector Array Camera and Spectrometer (PACS) instrument. Full details of the observing strategy can be found in Groves et al. (2012). The maps cover an area of roughly $1^\circ \times 3^\circ$. The FWHM angular resolution of the $70\ \mu\text{m}$ and $160\ \mu\text{m}$ maps is $5.6''$ and $11.4''$, respectively.

Smith et al. (2012) constructed the dust temperature map of M31 via pixel-by-pixel analysis of Spitzer and Herschel maps in the wavelength range $70\text{--}500\ \mu\text{m}$. All of the maps were convolved to the resolution of Herschel $500\ \mu\text{m}$ map that has the largest FWHM resolution ($36''$). The dust temperature for each pixel was measured by fitting a FIR through submillimeter spectral energy distribution with a single-temperature modified blackbody model: $S_\nu = \kappa_\nu M_{\text{dust}} B(\nu, T_{\text{dust}})/D^2$, where κ_ν is the dust absorption coefficient described by a power law with dust emissivity index β such that $\kappa_\nu \propto \nu^\beta$, M_{dust} is the dust mass with dust temperature T_{dust} , $B(\nu, T_{\text{dust}})$ is the Planck function, and D is the distance to the galaxy. The estimated uncertainty in the dust temperature is 1.4 K. The dust temperature was measured where the fluxes in all six bands (five Herschel and MIPS $70\ \mu\text{m}$) had a signal-to-noise ratio greater than 3σ .

The total star formation rate map of M31 (dust-obscured and unobscured) was constructed from the GALEX FUV and Spitzer $24\ \mu\text{m}$ maps by Ford et al. (2013). The contribution from the giant stellar population at $24\ \mu\text{m}$ was removed using the IRAC Spitzer $3.6\ \mu\text{m}$ band (see also Section 4.1).

We also used the optically identified H II region catalog of Azimlu et al. (2011) for this study. Azimlu et al. (2011) used the data from the Nearby Galaxies Survey of Massey et al. (2006), which includes H α and R-band mosaics of ten overlapping fields across the disk of M31. Azimlu et al. (2011) identified 3961 H II regions above a 10σ H α flux limit of $10^{-16}\ \text{erg cm}^{-2}\ \text{s}^{-1}$.

Finally, we obtained Wide-field Infrared Survey Explorer (WISE) maps of M31 at $3.4\ \mu\text{m}$ (Figure 3, top) and $22\ \mu\text{m}$ from the NASA/IPAC Infrared Science Archive³. WISE mapped the sky in four bands at 3.4 , 4.6 , 12 , and $22\ \mu\text{m}$ with an angular resolution of $6.1''$, $6.4''$, $6.5''$, and $12.0''$, respectively (Wright et al. 2010).

3.2. Photometry

Photometric measurements at $24\ \mu\text{m}$, $70\ \mu\text{m}$, and $160\ \mu\text{m}$ were performed using the Aperture Photometry Tool (APT, Laher et al. 2012). The point spread function (PSF) FWHM of the $24\ \mu\text{m}$, $70\ \mu\text{m}$, and $160\ \mu\text{m}$ images is $6''$, $5.6''$, and $11.4''$, respectively, and the pixel size is $1.24''$, $3.2''$, and $6.4''$. We select aperture radii of $6.2''$, $6.4''$, and $6.4''$. We chose similar aperture sizes at all wavelengths in order to match physical sizes in the photometry.

We performed aperture photometry on the SFR map using an aperture radius of $6''$. The dust temperatures were obtained from the dust temperature map at each $24\ \mu\text{m}$ source position (Figure 1). Five regions did not meet the 3σ dust temperature threshold (Section 3.1) and were therefore omitted from the analysis sample (Section 4).

Due to crowding in the molecular ring, estimation of the local background is difficult. We subtract a local non-annulus sky background using the default ‘‘Model F’’ algorithm in the APT that estimates the sky background using bilinear interpolation of the mode statistic. This model has been suggested for photometry in crowded fields (Laher et al. 2012).

Although re-scaling all maps to the largest resolution of $11.4''$ at $160\ \mu\text{m}$ would be appropriate to obtain photometry over a uniform physical scale, we chose to perform photometry at the original resolution of the maps. This is due to the fact that the resolution of $24\ \mu\text{m}$, $70\ \mu\text{m}$, and SFR maps are similar and in the range $5.6''\text{--}6''$. Since the objects are in a crowded field, re-scaling the maps to a larger resolution would lead to (additional) confusion.

We obtained the encircled energy fraction (EEF) for the Herschel images from the PACS Photometer Point-Source Flux Calibration document⁴; the estimated aperture correction factor ($1/\text{EEF}$) for aperture radii of $\sim 6.4''$ ($70\ \mu\text{m}$) and $\sim 6.4''$ ($160\ \mu\text{m}$) corresponds to ~ 1.56 and 2.6 , respectively. For the $24\ \mu\text{m}$ map, we adopt an aperture correction factor of ~ 1.61 for the $6''$ aperture radius⁵.

The uncertainties assigned to the measured photometric flux densities correspond to the standard deviation of the photometric flux of a large number of blank sources in each image. We obtain aperture photometric flux for 50 blank sky locations and measure the standard deviation of the photometric flux of the blank sources; this gives a good measure of the true photometric error of the

³ <http://hachi.ipac.caltech.edu:8080/montage>

⁴ http://herschel.esac.esa.int/twiki/pub/Public/PacsCalibrationWeb/pacs_bolo_fluxcal_report_v1.pdf

⁵ <http://irsa.ipac.caltech.edu/data/SPITZER/docs/mips/mipsinstrumenthandbook/50/>

Table 2. Multi-Wavelength Properties of Water Maser Hosts in M31

Maser (J2000)	T_{dust} (K)	$\log(\text{SFR})$ ($M_{\odot} \text{ yr}^{-1}$)	$\log(24 \mu\text{m})$ (Jy)	$\log(70 \mu\text{m})$ (Jy)	$\log(160 \mu\text{m})$ (Jy)	$\log(\text{H}\alpha)$ (mW m^{-2})	H_2O (mJy km s^{-1})	$L_{\text{H}_2\text{O}}$ (L_{\odot})	$\log(L_{\text{TIR}})$ (L_{\odot})
003918.9+402158.4	23.0	-4.1203(7)	-1.2372(7)	-0.136(10)	0.096(7)	-12.485(1)	447(43)	0.0063(6)	6.102(5)
004121.7+404947.7	18.3	-4.3142(11)	-1.3780(10)	-0.273(14)	0.270(5)	-13.445(66)	95(20)	0.0013(3)	6.139(5)
004343.9+411137.6	19.4	-4.3600(12)	-1.4511(12)	-0.413(19)	0.124(7)	-13.496(30)	58(9)	0.00081(13)	6.003(6)
004409.5+411856.6	18.4	-4.8241(35)	-1.8660(32)	-0.466(21)	-0.097(11)	< -16	82(14)	0.0011(2)	5.811(10)
004430.5+415154.8	22.6	-3.9200(4)	-0.9897(4)	0.097(6)	0.361(4)	-12.370(2)	67(15)	0.0009(2)	6.353(3)

NOTE—The integrated H_2O maser flux densities and luminosities were obtained from Darling (2011). Parenthetical values indicate 1σ statistical uncertainties. The 1σ uncertainties for photometric flux densities and SFR indicate statistical uncertainties for images with high signal to noise ratios, but the systematic uncertainties are likely to be higher.

targets. The estimated 1σ uncertainties in the $24 \mu\text{m}$, $70 \mu\text{m}$, and $160 \mu\text{m}$ maps correspond to 1.16×10^{-4} , 0.0168, 0.0186 Jy, respectively. The 1σ uncertainty for star formation rate corresponds to $1.2 \times 10^{-7} M_{\odot} \text{ yr}^{-1}$. The 1σ uncertainties for photometric flux densities and SFR represent statistical uncertainties for images with high signal to noise ratios, and the systematic uncertainties are likely to be higher. Measured flux densities and SFR for the water maser and non-maser sample regions are shown in Table 2 and Table 3, respectively.

The multi-wavelength data used in this work were obtained at different resolutions. While the resolution of the Spitzer and Herschel maps ranges from $5.6''$ to $11.4''$, the resolution of the dust temperature map is $\sim 36''$ based on the resolution of Herschel maps at longer wavelengths (e.g., $500 \mu\text{m}$, Smith et al. 2012). Additionally, the crowded field and the large PSF of Spitzer and Herschel maps ($5.6''$ – $11.4''$) may introduce contamination from nearby or confused sources (e.g., Calzetti et al. 2005).

Table 3. Multi-Wavelength Properties of the Non-Maser Sample

Object (J2000)	T_{dust} (K)	$\log(\text{SFR})$ ($M_{\odot} \text{ yr}^{-1}$)	$\log(24 \mu\text{m})$ (Jy)	$\log(70 \mu\text{m})$ (Jy)	$\log(160 \mu\text{m})$ (Jy)	$\log(\text{H}\alpha)$ (mW m^{-2})	$\log(L_{\text{TIR}})$ (L_{\odot})
003852.5+401904.9	...	-5.0137(54)	-2.0871(53)	< -1.3	< -1.2	< -16	...
003904.8+402927.4	15.8	-5.1991(82)	-2.2906(85)	-1.276(137)	-0.757(50)	-14.149(21)	5.133(45)
003906.7+403704.5	21.7	-4.8866(40)	-2.0037(44)	-0.914(59)	-0.458(25)	-14.613(18)	5.446(21)
003909.8+402705.0	17.4	-5.0078(53)	-2.3951(108)	< -1.3	-0.724(46)	-13.146(3)	...
003910.2+403725.6	21.3	-4.1747(8)	-1.2574(8)	-0.189(11)	0.116(7)	-13.157(1)	6.091(4)
003914.6+404157.9	18.3	-5.2161(86)	-2.3364(94)	< -1.3	-0.749(49)	-13.668(5)	...
003916.1+403629.5	19.6	-4.5794(20)	-1.6420(19)	-0.536(25)	-0.331(19)	< -16	5.690(12)
003930.2+402106.4	18.7	-4.6986(26)	-1.8281(29)	-0.634(31)	-0.302(17)	-13.788(9)	5.642(13)
003933.2+402215.6	20.0	-4.6260(22)	-1.6942(21)	< -1.3	-1.200(138)	-14.827(56)	...
003935.2+404814.6	20.8	-5.1970(82)	-2.2735(82)	-1.094(90)	-0.649(39)	< -16	5.249(34)
003937.5+402011.5	19.3	-4.6986(26)	-1.8081(28)	-0.633(31)	-0.316(18)	-13.186(7)	5.637(14)
003938.9+401921.3	17.3	-4.8657(38)	-2.2223(72)	-1.073(86)	-0.468(26)	-13.094(5)	5.376(25)
003939.1+405018.3	20.0	-4.8583(38)	-2.3715(102)	-1.210(117)	-0.673(41)	-12.971(10)	5.193(39)
003939.8+402856.3	19.2	-4.8718(39)	-2.0533(49)	-0.956(65)	-0.345(19)	-13.396(6)	5.502(19)
003941.5+402133.7	19.8	-4.8948(41)	-1.9579(39)	-0.774(43)	-0.286(17)	-13.044(7)	5.595(15)
003941.9+402045.6	21.3	-4.5207(17)	-1.6223(18)	-0.482(22)	-0.014(9)	-13.481(10)	5.879(8)
003943.0+402039.9	22.1	-4.5212(17)	-1.6207(18)	-0.483(22)	-0.017(9)	-13.025(3)	5.877(8)
003944.5+402030.4	22.1	-4.5685(19)	-1.6340(19)	-0.565(27)	0.035(8)	-13.572(3)	5.889(7)
003945.2+402058.0	21.1	-4.6134(21)	-1.9717(41)	-0.660(33)	0.033(8)	-13.623(4)	5.840(8)
003948.5+403113.1	20.3	-5.0259(55)	-2.0985(54)	-1.260(132)	-0.840(60)	< -16	5.124(46)
003950.5+402305.9	17.0	-5.0805(63)	-2.1686(64)	< -1.3	-1.089(107)	-14.889(66)	...
003951.3+405306.1	20.9	-5.0345(56)	-2.3009(87)	-1.256(130)	-0.750(49)	< -16	5.141(44)
003956.8+402437.6	18.2	-5.0229(55)	-2.0963(54)	< -1.3	-1.192(135)	< -16	...
004000.3+405318.6	20.6	-4.9684(48)	-2.0428(48)	< -1.3	< -1.2	< -16	...

Table 3 continued

Table 3 (*continued*)

Object (J2000)	T_{dust} (K)	$\log(\text{SFR})$ ($M_{\odot} \text{ yr}^{-1}$)	$\log(24 \mu\text{m})$ (Jy)	$\log(70 \mu\text{m})$ (Jy)	$\log(160 \mu\text{m})$ (Jy)	$\log(\text{H}\alpha)$ (mW m^{-2})	$\log(L_{\text{TIR}})$ (L_{\odot})
004004.7+405840.9	20.4	-4.9670(48)	-2.0378(47)	-0.984(70)	-0.349(19)	-14.686(118)	5.495(19)
004010.4+404517.7	17.9	-4.9096(42)	-1.9919(43)	-0.893(57)	-0.478(26)	-14.174(56)	5.442(22)
004020.3+403124.5	18.1	-4.9174(43)	-1.9794(41)	< -1.3	< -1.2	< -16	...
004020.5+403723.9	18.1	-5.2107(85)	-2.2355(75)	< -1.3	-0.607(35)	< -16	...
004023.8+403904.4	18.9	-4.9036(42)	-1.9910(43)	-0.933(62)	-0.327(18)	-13.951(7)	5.526(18)
004026.2+403706.5	18.9	-5.2147(85)	-2.2871(84)	< -1.3	-0.906(70)	< -16	...
004030.9+404230.0	17.0	-4.5410(18)	-1.8839(33)	-0.827(49)	-0.216(14)	-13.033(1)	5.635(14)
004031.2+403952.0	18.2	-4.9117(43)	-1.9490(39)	-0.863(53)	-0.018(9)	-13.936(9)	5.768(10)
004031.3+404032.8	17.3	-5.2423(91)	-2.2725(81)	< -1.3	-0.369(20)	< -16	...
004031.7+404127.0	16.4	-4.2980(10)	-1.3721(10)	-0.495(23)	0.076(7)	-13.987(6)	5.967(6)
004032.5+405127.4	18.8	-5.1058(66)	-2.1953(68)	-1.100(91)	-0.335(19)	-13.710(12)	5.469(20)
004032.6+403856.1	19.6	-4.6623(24)	-1.7210(23)	-0.493(23)	0.081(7)	-13.252(2)	5.928(7)
004032.7+403531.2	19.4	-5.0530(59)	-2.0928(54)	-1.296(143)	0.194(6)	-13.708(105)	5.908(7)
004032.7+403936.5	18.2	-4.8785(39)	-1.9146(36)	-0.805(46)	0.061(8)	-13.987(13)	5.841(8)
004032.7+410045.1	17.3	-5.3674(121)	-2.4312(117)	< -1.3	< -1.2	< -16	...
004032.8+405540.2	16.3	-5.0700(61)	-2.2246(73)	< -1.3	-0.466(25)	-13.955(10)	...
004032.9+403919.2	19.4	-4.9752(49)	-2.0102(44)	-0.801(46)	-0.033(9)	-13.283(3)	5.762(10)
004033.0+404102.8	17.1	-4.9738(49)	-2.0789(52)	-1.085(88)	0.075(7)	-14.004(5)	5.813(9)
004033.3+403352.1	18.5	-5.0363(57)	-2.2029(69)	< -1.3	-0.731(47)	-14.812(152)	...
004033.8+403246.6	18.0	-4.9641(48)	-2.0601(50)	-1.031(78)	-0.367(20)	-13.107(7)	5.471(20)
004034.7+403541.2	19.4	-3.6741(2)	-0.7434(2)	0.020(7)	0.194(6)	-13.199(1)	6.316(2)
004035.1+403701.1	18.0	-4.7383(29)	-1.8454(30)	-0.949(64)	-0.128(12)	-13.450(4)	5.681(12)
004035.8+403724.6	17.3	-4.8373(36)	-1.9735(41)	< -1.3	-0.172(13)	-13.652(4)	...
004036.0+403821.0	18.2	-5.2656(96)	-2.2683(81)	< -1.3	-0.335(19)	-14.690(18)	...
004036.1+410117.5	16.6	-4.5897(20)	-1.8208(29)	-0.692(36)	-0.221(14)	-13.433(14)	5.672(13)
004036.3+403641.9	18.0	-5.0530(59)	-2.1601(63)	-1.197(114)	-0.098(11)	< -16	5.651(13)
004036.3+405329.3	16.9	-5.2472(92)	-2.3045(88)	-0.950(65)	-0.405(22)	< -16	5.442(22)
004036.8+403557.1	18.6	-4.8963(41)	-2.0184(45)	-1.047(81)	0.002(9)	-14.510(17)	5.757(10)
004038.0+403514.9	18.4	-4.4850(16)	-1.5286(15)	-0.483(22)	0.199(5)	-14.372(53)	6.030(5)
004038.0+404728.3	18.9	-5.1033(66)	-2.2137(71)	-1.059(83)	-0.473(26)	< -16	5.377(25)
004038.6+403814.7	17.8	-5.4021(132)	-2.4134(113)	< -1.3	-0.244(15)	< -16	...
004038.7+403533.2	17.6	-4.8419(36)	-1.8899(34)	-0.874(54)	0.209(5)	< -16	5.956(6)
004038.8+403431.0	18.4	-4.8352(36)	-1.8858(33)	-0.857(52)	-0.177(13)	-13.983(29)	5.656(13)
004039.4+403730.5	18.1	-4.5212(17)	-1.5971(17)	-0.564(27)	-0.004(9)	-13.071(1)	5.868(8)
004039.7+403457.9	18.4	-4.8093(34)	-1.8909(34)	-0.835(49)	0.031(8)	-14.210(38)	5.815(9)
004041.6+405105.0	16.8	-4.6675(24)	-1.7385(24)	-0.746(40)	-0.298(17)	-13.575(6)	5.623(14)
004042.1+403454.5	18.5	-4.8034(33)	-1.8753(33)	-0.931(62)	-0.143(12)	-14.640(115)	5.669(13)
004043.3+404321.9	17.1	-4.8259(35)	-1.9133(36)	-1.278(137)	-0.244(15)	-13.502(62)	5.545(17)
004043.6+403530.5	18.1	-4.7494(29)	-1.8183(29)	-0.758(41)	0.024(8)	-14.130(90)	5.827(9)
004043.7+405251.5	16.4	-5.1273(70)	-2.2179(72)	-1.050(81)	-0.284(17)	< -16	5.514(18)
004044.2+404446.4	19.0	-4.8138(34)	-1.8754(33)	-0.815(47)	-0.307(18)	< -16	5.581(16)
004045.7+405134.5	17.0	-4.9567(47)	-2.0458(48)	< -1.3	-0.717(45)	-15.036(58)	...
004046.4+405541.9	18.1	-4.8493(37)	-1.9529(39)	-0.698(36)	0.014(8)	-14.441(26)	5.820(9)
004046.5+405606.4	17.8	-4.7975(33)	-1.9031(35)	-0.720(38)	0.079(7)	< -16	5.869(8)
004047.3+405903.2	18.2	-4.8531(37)	-2.0461(48)	-0.920(60)	-0.294(17)	-12.975(7)	5.546(17)
004050.0+405938.5	18.0	-5.0748(62)	-2.1373(60)	-1.231(123)	-0.242(15)	-14.467(123)	5.529(18)
004051.6+410006.5	17.7	-4.7461(29)	-1.8147(28)	-0.768(42)	-0.250(15)	< -16	5.635(14)
004051.7+403602.3	19.3	-4.9489(46)	-2.1118(56)	-0.983(70)	-0.340(19)	-12.851(1)	5.495(19)
004051.9+403249.7	18.1	-4.9980(52)	-2.0466(48)	-1.193(113)	-0.059(10)	-13.166(11)	5.691(12)
004053.0+403218.0	19.7	-4.5697(19)	-1.6511(19)	-0.482(22)	-0.058(10)	-13.220(7)	5.849(8)

Table 3 continued

Table 3 (*continued*)

Object (J2000)	T_{dust} (K)	$\log(\text{SFR})$ ($M_{\odot} \text{ yr}^{-1}$)	$\log(24 \mu\text{m})$ (Jy)	$\log(70 \mu\text{m})$ (Jy)	$\log(160 \mu\text{m})$ (Jy)	$\log(\text{H}\alpha)$ (mW m^{-2})	$\log(L_{\text{FIR}})$ (L_{\odot})
004055.1+403703.2	17.2	-4.8166(34)	-1.8758(33)	-0.784(44)	0.059(8)	-14.013(7)	5.845(8)
004057.3+403607.0	18.1	-5.0378(57)	-2.1386(60)	-1.134(99)	-0.453(25)	-13.088(2)	5.383(25)
004058.2+410302.3	19.2	-4.2468(9)	-1.9107(35)	-0.811(47)	0.364(4)	-12.879(5)	6.096(4)
004058.3+403711.1	17.6	-4.9494(46)	-2.0484(49)	-0.967(67)	0.030(8)	-14.208(8)	5.788(10)
004058.4+405325.2	16.4	-5.0965(65)	-2.1595(63)	-1.110(93)	< -1.2	< -16	...
004058.4+410217.9	17.6	-4.8449(36)	-1.9903(42)	-1.012(74)	-0.093(11)	-14.399(104)	5.686(12)
004058.4+410225.9	17.6	-4.8338(36)	-1.9963(43)	-0.930(62)	-0.053(10)	< -16	5.727(11)
004058.6+404558.0	18.2	-4.6946(26)	-1.7511(24)	-0.622(30)	-0.051(10)	-12.801(17)	5.806(9)
004058.6+410332.3	20.9	-3.6064(2)	-0.6795(2)	0.169(5)	0.378(4)	-12.752(1)	6.453(2)
004059.1+410233.1	19.2	-4.8310(35)	-1.9989(43)	-0.930(62)	-0.052(10)	-13.260(15)	5.728(11)
004059.8+403652.4	17.6	-4.5892(20)	-1.6366(19)	-0.670(34)	0.132(6)	-13.439(2)	5.938(7)
004100.6+410334.0	17.8	-4.6688(24)	-1.7725(26)	-0.671(34)	0.364(4)	-13.793(66)	6.115(4)
004101.6+410405.8	19.3	-4.2222(9)	-1.3013(9)	-0.208(12)	0.239(5)	-13.611(3)	6.147(4)
004102.0+410254.9	18.1	-4.6330(22)	-1.8014(27)	-0.703(37)	-0.164(13)	-12.967(8)	5.708(12)
004102.3+410431.7	18.1	-4.8480(37)	-1.9528(39)	-0.811(47)	0.242(5)	-12.928(6)	5.988(6)
004102.7+410344.5	19.3	-4.8935(41)	-2.0109(45)	-0.911(59)	0.054(8)	-13.701(44)	5.816(9)
004103.1+403749.9	16.6	-5.0492(58)	-2.1373(60)	-1.069(85)	0.081(7)	< -16	5.817(9)
004104.8+410534.6	17.3	-4.9341(45)	-1.9993(43)	-1.250(129)	-0.008(9)	-14.284(108)	5.734(11)
004107.2+410410.0	17.4	-4.8947(41)	-1.9633(40)	-0.813(47)	-0.098(11)	-13.450(17)	5.715(11)
004107.6+404812.5	17.2	-5.0002(52)	-2.1018(55)	-0.902(58)	-0.359(20)	-13.854(82)	5.501(19)
004108.6+410437.9	16.0	-5.1169(68)	-2.1628(63)	< -1.3	-0.248(15)	< -16	...
004109.1+404852.7	18.7	-4.8498(37)	-2.1523(62)	< -1.3	-0.478(26)	-13.987(39)	...
004109.2+404910.3	18.7	-4.8232(35)	-2.0789(52)	-0.886(56)	-0.215(14)	-13.092(35)	5.606(15)
004110.4+404949.5	18.7	-4.7949(32)	-2.0170(45)	-0.902(58)	-0.267(16)	-14.359(144)	5.571(16)
004110.6+410516.4	16.0	-4.9482(46)	-2.0707(51)	-1.092(89)	-0.013(9)	< -16	5.737(11)
004112.5+410609.7	17.1	-4.8372(36)	-1.9844(42)	-1.093(90)	-0.291(17)	-13.928(45)	5.523(18)
004113.7+403918.6	17.0	-4.6970(26)	-1.7407(24)	-0.799(46)	-0.273(16)	-14.148(85)	5.625(14)
004113.8+410814.6	17.1	-5.0928(65)	-2.2015(69)	-1.171(107)	-0.329(19)	-13.708(15)	5.462(21)
004113.9+410736.1	18.2	-4.7384(29)	-1.8575(31)	-0.789(45)	-0.168(13)	-12.883(4)	5.679(12)
004114.8+410923.7	19.8	-4.1148(7)	-1.1781(7)	-0.253(13)	-0.044(10)	-12.967(3)	6.011(5)
004115.9+404011.6	16.7	-4.6970(26)	-1.7379(24)	< -1.3	-0.514(28)	-14.775(10)	...
004119.1+404857.4	17.0	-4.8820(40)	-1.9441(38)	-0.889(56)	-0.223(15)	-13.775(87)	5.612(15)
004119.5+411948.8	25.9	-4.0676(6)	-1.1560(6)	-0.209(12)	0.015(8)	-12.810(2)	6.057(5)
004120.0+410821.5	19.0	-4.6307(22)	-1.7401(24)	-0.725(38)	-0.306(18)	-12.936(3)	5.625(14)
004120.9+403414.0	17.2	-5.2089(84)	-2.3551(98)	< -1.3	-1.206(139)	-14.688(177)	...
004121.2+411947.8	22.6	-4.7685(31)	-1.9945(43)	-0.814(47)	-0.424(23)	-12.851(2)	5.496(19)
004123.2+405000.6	17.4	-4.7072(27)	-1.7831(26)	-0.877(55)	0.270(5)	-14.498(261)	6.015(5)
004124.1+411124.1	18.1	-5.0143(54)	-2.0723(51)	-1.122(96)	-0.287(17)	-14.757(57)	5.513(18)
004124.8+411154.6	19.6	-4.6842(25)	-1.7563(25)	-0.693(36)	-0.013(9)	-13.498(15)	5.817(9)
004125.4+404200.4	19.7	-4.4886(16)	-1.5463(15)	-0.508(23)	-0.131(12)	-13.260(50)	5.814(9)
004126.1+404959.1	18.4	-4.3855(13)	-1.4544(12)	-0.379(17)	0.226(5)	-14.344(220)	6.078(5)
004126.5+411206.9	20.0	-4.6575(24)	-1.7475(24)	-0.627(31)	-0.013(9)	-12.924(5)	5.831(9)
004127.3+404242.7	17.5	-5.0301(56)	-2.1059(55)	-0.980(69)	-0.326(18)	-14.270(139)	5.506(19)
004128.1+404155.2	18.4	-5.2359(90)	-2.3437(96)	-1.260(132)	-0.234(15)	< -16	5.519(18)
004128.1+411222.6	20.1	-4.6160(22)	-1.6984(22)	-0.648(32)	0.042(8)	-12.991(5)	5.870(8)
004129.2+411242.8	20.1	-4.8076(33)	-1.8738(32)	-0.736(39)	0.042(8)	-13.951(19)	5.839(8)
004129.3+404218.9	17.7	-5.1215(69)	-2.2005(69)	-1.128(97)	-0.239(15)	< -16	5.539(17)
004129.5+411006.3	18.7	-4.9730(49)	-2.0674(51)	-0.784(44)	-0.406(22)	-13.866(8)	5.508(19)
004129.8+405059.5	21.3	-3.9712(5)	-1.0747(5)	-0.022(8)	0.268(5)	-12.666(2)	6.253(3)
004130.3+410501.7	19.0	-3.9371(5)	-1.0201(5)	0.057(6)	0.319(4)	-12.354(2)	6.314(2)

Table 3 *continued*

Table 3 (*continued*)

Object (J2000)	T_{dust} (K)	$\log(\text{SFR})$ ($M_{\odot} \text{ yr}^{-1}$)	$\log(24 \mu\text{m})$ (Jy)	$\log(70 \mu\text{m})$ (Jy)	$\log(160 \mu\text{m})$ (Jy)	$\log(\text{H}\alpha)$ (mW m^{-2})	$\log(L_{\text{TIR}})$ (L_{\odot})
004131.9+411331.5	18.3	-4.9180(43)	-2.0137(45)	-0.923(61)	-0.205(14)	-13.959(12)	5.612(15)
004135.7+405009.3	17.6	-5.1077(67)	-2.1527(62)	-1.289(141)	-0.747(48)	< -16	5.158(42)
004136.9+403805.6	19.5	-4.9912(51)	-2.0671(51)	-1.254(130)	-1.000(87)	< -16	5.058(53)
004137.0+405142.5	16.8	-4.6495(23)	-1.7157(23)	-0.950(64)	-0.358(20)	-14.854(118)	5.545(17)
004138.6+404401.2	19.7	-4.6785(25)	-1.7951(27)	-0.699(36)	-0.130(12)	-12.951(8)	5.731(11)
004141.3+411916.7	16.0	-5.1303(70)	-2.1881(67)	< -1.3	-0.115(11)	< -16	...
004143.6+410840.1	17.0	-5.0470(58)	-2.1161(57)	-1.058(83)	-0.222(14)	-14.210(27)	5.568(16)
004144.6+411658.1	17.7	-5.0956(65)	-2.1717(64)	-1.224(121)	-0.185(13)	< -16	5.574(16)
004145.0+404746.4	17.7	-4.9709(49)	-2.0448(48)	< -1.3	< -1.2	< -16	...
004146.7+411846.6	18.9	-4.6121(21)	-1.7417(24)	-0.585(28)	-0.122(12)	-12.947(2)	5.771(10)
004147.4+411942.4	16.5	-5.1915(81)	-2.3001(87)	-1.228(122)	0.106(7)	-14.772(32)	5.824(9)
004148.2+411903.8	19.0	-4.3218(11)	-1.3927(11)	-0.268(13)	0.104(7)	-13.114(4)	6.039(5)
004149.6+411953.8	16.9	-5.2779(99)	-2.3961(108)	< -1.3	-0.602(35)	< -16	...
004151.3+412500.7	20.8	-5.0847(63)	-2.1337(59)	0.055(6)	0.073(7)	< -16	6.114(4)
004151.6+404620.5	18.3	-5.1313(71)	-2.1919(68)	-1.022(76)	-0.753(49)	-13.620(18)	5.224(36)
004151.9+412442.1	25.8	-4.2024(8)	-1.2639(8)	0.055(6)	0.070(7)	< -16	6.168(4)
004154.5+404718.9	19.7	-4.9073(42)	-1.9634(40)	-0.844(51)	-0.311(18)	-13.300(14)	5.560(16)
004159.4+405720.8	18.0	-4.5676(19)	-1.6330(19)	-0.919(60)	-0.346(19)	-13.686(28)	5.576(16)
004200.6+404747.8	21.2	-5.0073(53)	-2.1219(57)	-0.976(68)	-0.747(49)	-13.569(15)	5.254(34)
004200.9+405217.2	16.1	-5.0346(56)	-2.1036(55)	-1.053(82)	-0.536(30)	< -16	5.350(27)
004202.4+412436.0	18.4	-4.9840(50)	-2.0250(46)	-0.709(37)	-0.208(14)	< -16	5.656(13)
004202.9+412232.4	16.5	-4.8582(38)	-2.0021(44)	-0.868(53)	-0.163(13)	-13.049(9)	5.654(13)
004203.9+404907.1	23.1	-4.0290(6)	-1.0996(5)	-0.316(15)	-0.324(18)	-13.250(12)	5.915(7)
004204.9+404936.6	20.0	-5.1155(68)	-2.1822(66)	-1.179(109)	-0.561(32)	-14.000(33)	5.295(31)
004206.7+405621.5	19.3	-5.3461(116)	-2.4010(109)	-1.176(108)	-0.572(32)	< -16	5.266(33)
004208.5+405720.2	18.7	-5.2828(100)	-2.3433(96)	< -1.3	-0.517(29)	< -16	...
004208.5+412409.8	18.0	-4.8340(36)	-1.9687(40)	-0.997(72)	-0.186(13)	-13.246(5)	5.618(14)
004208.7+405052.1	17.6	-5.0517(59)	-2.2696(81)	-1.168(106)	-0.472(26)	-13.854(40)	5.350(27)
004208.8+412639.9	17.8	-4.8986(41)	-1.9495(39)	-0.627(31)	-0.156(12)	< -16	5.719(11)
004209.0+412442.3	17.0	-5.2765(99)	-2.3537(98)	< -1.3	-0.184(13)	< -16	...
004209.5+412705.5	18.7	-4.9979(52)	-2.0377(47)	-0.903(58)	-0.383(21)	< -16	5.491(19)
004209.5+412832.3	22.3	-4.5198(17)	-1.7806(26)	-0.791(45)	-0.505(28)	-12.573(2)	5.494(19)
004209.8+412412.2	18.0	-4.8352(36)	-1.9809(42)	-1.233(124)	-0.186(13)	< -16	5.588(15)
004210.3+412529.3	17.6	-5.3537(118)	-2.4977(137)	< -1.3	-0.437(24)	< -16	...
004211.2+412442.6	17.0	-5.0260(55)	-2.1067(56)	-0.983(70)	-0.251(15)	< -16	5.559(16)
004211.6+411909.4	16.2	-4.9511(47)	-2.0430(48)	< -1.3	-0.835(59)	< -16	...
004212.3+412415.7	18.9	-4.6636(24)	-1.7302(23)	-0.569(27)	0.026(8)	-13.455(6)	5.872(8)
004213.8+405117.7	21.8	-3.9660(5)	-1.0332(5)	-0.011(7)	0.304(4)	-12.879(5)	6.282(3)
004214.8+412508.9	17.0	-4.8203(34)	-1.9001(35)	-1.005(73)	-0.266(16)	< -16	5.566(16)
004218.1+412631.1	18.5	-5.2643(96)	-2.4399(120)	< -1.3	-0.092(11)	< -16	...
004218.7+412751.8	19.6	-4.5814(20)	-1.6802(21)	-0.506(23)	0.069(7)	-13.442(9)	5.921(7)
004220.6+412749.0	19.6	-4.7532(30)	-1.7849(26)	-0.624(30)	0.022(8)	-13.801(11)	5.853(8)
004221.7+412827.6	18.0	-4.8411(36)	-1.9242(36)	-0.941(63)	-0.275(16)	-13.105(4)	5.568(16)
004224.8+412758.7	17.4	-4.8104(34)	-1.8328(30)	-0.908(59)	0.237(5)	< -16	5.981(6)
004225.9+412831.9	18.5	-4.3799(12)	-1.4245(12)	-0.566(27)	0.237(5)	-13.796(22)	6.055(5)
004226.4+412811.2	18.5	-4.3787(12)	-1.4239(12)	-0.324(15)	0.234(5)	-13.138(6)	6.099(4)
004227.6+412019.6	17.1	-4.9403(45)	-2.0093(44)	-1.037(79)	-0.007(9)	< -16	5.751(10)
004229.8+410550.6	17.8	-4.9933(51)	-2.0677(51)	< -1.3	-0.483(26)	< -16	...
004230.3+412935.9	18.1	-4.4036(13)	-1.4534(12)	-0.547(26)	0.047(8)	-14.086(16)	5.925(7)
004232.1+412936.5	18.1	-4.7609(30)	-1.7899(27)	-0.685(35)	0.103(7)	-13.253(11)	5.901(7)

Table 3 *continued*

Table 3 (*continued*)

Object (J2000)	T_{dust} (K)	$\log(\text{SFR})$ ($M_{\odot} \text{ yr}^{-1}$)	$\log(24 \mu\text{m})$ (Jy)	$\log(70 \mu\text{m})$ (Jy)	$\log(160 \mu\text{m})$ (Jy)	$\log(\text{H}\alpha)$ (mW m^{-2})	$\log(L_{\text{TIR}})$ (L_{\odot})
004232.3+413008.7	17.5	-4.8906(41)	-1.9325(37)	-1.161(105)	0.106(7)	-14.924(84)	5.843(8)
004232.7+411143.6	...	-5.3053(105)	-2.3473(97)	< -1.3	< -1.2	< -16	...
004234.2+413007.3	17.7	-4.4638(15)	-1.5313(15)	-0.501(23)	0.083(7)	-13.223(9)	5.947(6)
004235.0+404838.1	23.1	-5.0910(64)	-2.1851(67)	< -1.3	< -1.2	< -16	...
004235.3+413224.4	17.8	-5.0919(64)	-2.1734(65)	-1.274(136)	0.133(6)	-14.228(23)	5.850(8)
004235.6+413149.0	19.0	-4.7666(30)	-1.8362(30)	-0.673(34)	-0.004(9)	-13.375(9)	5.820(9)
004236.4+413308.7	15.9	-5.1835(80)	-2.3105(89)	< -1.3	-0.485(27)	-13.462(5)	...
004236.9+410158.0	16.6	-5.0839(63)	-2.1060(55)	-1.147(102)	-0.142(12)	-14.991(232)	5.622(14)
004238.6+413150.5	19.1	-4.5078(17)	-1.5925(17)	-0.561(26)	0.131(6)	< -16	5.961(6)
004238.9+413135.6	17.3	-4.7762(31)	-1.8391(30)	-0.561(26)	0.130(6)	-14.182(30)	5.940(7)
004240.1+410222.7	18.7	-4.6809(25)	-1.7315(23)	-0.607(29)	-0.062(10)	-12.886(3)	5.805(9)
004240.9+405910.8	16.0	-4.9355(45)	-1.9966(43)	-0.841(50)	-0.138(12)	-13.728(6)	5.677(12)
004241.3+412246.7	17.8	-4.2925(10)	-1.3573(10)	-0.348(16)	0.127(6)	-13.762(9)	6.035(5)
004241.7+413245.4	18.5	-4.8538(37)	-1.8662(32)	-0.711(37)	0.106(7)	-13.810(12)	5.894(7)
004242.1+410303.0	17.9	-5.1186(68)	-2.1651(64)	-1.128(97)	-0.329(19)	-13.090(4)	5.471(20)
004242.5+410001.4	17.2	-4.5526(19)	-1.6190(18)	-0.827(49)	-0.133(12)	< -16	5.728(11)
004242.5+413155.2	19.3	-4.3052(11)	-1.3642(10)	-0.226(12)	0.236(5)	-13.061(3)	6.132(4)
004242.9+413159.8	17.4	-4.2939(10)	-1.3604(10)	-0.228(12)	0.230(5)	-13.775(13)	6.128(4)
004244.1+413259.2	18.9	-4.4599(15)	-1.4949(14)	-0.531(25)	0.236(5)	-13.967(31)	6.051(5)
004244.9+413338.6	19.4	-4.2294(9)	-1.2794(8)	-0.223(12)	0.275(5)	-14.231(104)	6.167(4)
004245.0+405448.3	17.4	-4.8679(38)	-2.0234(46)	-1.237(125)	-0.821(58)	-13.181(3)	5.156(42)
004245.2+413316.7	18.9	-4.4582(15)	-1.4947(14)	-0.669(34)	0.249(5)	-13.714(19)	6.042(5)
004246.2+410111.4	17.4	-4.9162(43)	-1.9769(41)	-1.081(87)	-0.243(15)	-14.427(22)	5.561(16)
004246.8+414447.0	22.4	-4.7644(30)	-1.9148(36)	-0.879(55)	-0.917(72)	-13.959(108)	5.268(33)
004247.0+413333.0	19.7	-4.2327(9)	-1.2789(8)	-0.221(12)	0.274(5)	-13.005(3)	6.167(4)
004247.5+413131.1	17.0	-5.1923(81)	-2.2341(74)	< -1.3	-0.540(30)	< -16	...
004247.9+413400.5	19.7	-4.5666(19)	-1.6038(17)	-0.473(21)	0.074(7)	-13.848(37)	5.939(7)
004249.1+413440.0	17.7	-4.8955(41)	-1.9331(37)	-0.847(51)	-0.040(10)	< -16	5.754(10)
004249.3+412507.5	15.1	-4.6266(22)	-1.7000(22)	-0.772(43)	-0.181(13)	-13.356(5)	5.695(12)
004251.0+413507.8	17.7	-4.6313(22)	-1.6881(21)	-0.656(33)	-0.008(9)	-14.080(59)	5.834(8)
004252.3+410014.8	18.0	-4.6794(25)	-1.7523(25)	< -1.3	-0.620(36)	-14.772(98)	...
004252.4+410120.7	17.1	-4.9007(41)	-1.9617(40)	< -1.3	-0.447(24)	< -16	...
004253.0+413526.7	17.8	-4.8325(35)	-1.8767(33)	-0.673(34)	0.067(7)	-13.276(24)	5.869(8)
004253.5+413516.2	17.8	-4.8404(36)	-1.8742(33)	-0.670(34)	0.066(7)	-13.383(20)	5.869(8)
004254.4+405832.8	17.8	-5.1082(67)	-2.2066(70)	-1.070(85)	-0.409(22)	-13.544(8)	5.419(23)
004256.9+413728.1	22.6	-4.5297(18)	-1.6054(18)	-0.366(17)	0.199(5)	-14.189(42)	6.048(5)
004258.2+410015.9	17.4	-4.9696(49)	-2.0410(48)	-1.137(99)	-0.593(34)	< -16	5.304(30)
004258.8+413456.2	16.3	-5.1098(67)	-2.2563(78)	< -1.3	-0.505(28)	< -16	...
004259.1+413741.3	18.6	-4.5200(17)	-1.8336(30)	-0.663(33)	-0.113(11)	-13.367(21)	5.747(10)
004259.4+413722.5	21.8	-4.5188(17)	-1.8546(31)	-0.333(16)	0.324(4)	-13.315(14)	6.131(4)
004259.4+413732.1	21.8	-4.5192(17)	-1.8362(30)	-0.334(16)	0.325(4)	-14.094(46)	6.132(4)
004300.0+413526.2	17.1	-4.9433(46)	-2.0445(48)	-1.193(113)	-0.299(17)	-14.356(127)	5.497(19)
004300.0+413654.2	21.1	-4.3675(12)	-1.4221(11)	-0.216(12)	0.319(4)	-14.081(57)	6.181(4)
004301.0+413627.9	18.4	-4.9242(44)	-1.9954(43)	-0.829(49)	-0.049(10)	-13.395(14)	5.746(11)
004301.5+413717.2	21.8	-4.4017(13)	-1.4589(12)	-0.335(16)	0.264(5)	-14.210(61)	6.112(4)
004301.9+413655.2	19.1	-4.3668(12)	-1.4217(11)	-0.778(43)	0.322(4)	-13.839(48)	6.096(4)
004302.5+413740.5	20.8	-3.5479(2)	-0.6119(2)	0.332(3)	0.509(3)	-14.701(172)	6.578(1)
004302.5+414910.5	...	-4.6366(23)	-1.8250(29)	-1.211(118)	< -1.2	-13.343(24)	...
004303.4+413719.3	20.8	-3.5474(2)	-0.6119(2)	0.329(3)	0.512(3)	-12.889(15)	6.579(1)
004304.3+413739.5	20.8	-3.5479(2)	-0.6119(2)	0.332(3)	0.512(3)	-13.155(21)	6.580(1)

Table 3 *continued*

Table 3 (*continued*)

Object (J2000)	T_{dust} (K)	$\log(\text{SFR})$ ($M_{\odot} \text{ yr}^{-1}$)	$\log(24 \mu\text{m})$ (Jy)	$\log(70 \mu\text{m})$ (Jy)	$\log(160 \mu\text{m})$ (Jy)	$\log(\text{H}\alpha)$ (mW m^{-2})	$\log(L_{\text{TIR}})$ (L_{\odot})
004304.8+410554.0	19.0	-5.1441(73)	-2.2289(74)	< -1.3	-0.283(17)	< -16	...
004305.7+413749.8	19.1	-4.9538(47)	-2.0225(46)	0.332(3)	0.503(3)	-13.499(36)	6.462(2)
004306.7+410213.4	18.9	-5.3693(122)	-2.3868(106)	-1.290(141)	-0.627(37)	< -16	5.205(38)
004306.9+413807.1	19.1	-4.7052(26)	-1.7750(26)	-0.725(38)	-0.092(11)	-13.600(60)	5.753(10)
004308.2+410156.8	19.7	-5.2734(98)	-2.3351(94)	-1.054(82)	-0.516(29)	-13.500(20)	5.339(28)
004309.7+413849.3	19.1	-4.8369(36)	-1.9125(36)	-0.664(33)	-0.099(11)	-13.764(28)	5.749(10)
004310.5+410426.8	18.5	-5.0198(55)	-2.1048(55)	-1.238(125)	-0.232(15)	< -16	5.539(17)
004311.1+413743.3	18.7	-4.9448(46)	-2.0144(45)	-0.911(59)	-0.060(10)	-12.903(15)	5.724(11)
004311.3+410459.5	18.4	-4.4715(15)	-1.5473(15)	-0.640(32)	0.075(7)	-13.228(9)	5.912(7)
004311.6+411245.5	16.8	-5.2230(87)	-2.2793(83)	-1.238(125)	-1.022(91)	< -16	5.004(60)
004312.4+410125.2	21.7	-5.0241(55)	-2.2452(76)	-1.108(93)	-0.664(40)	-12.854(2)	5.239(35)
004312.5+413747.4	17.4	-5.1101(67)	-2.1758(65)	-0.915(59)	-0.059(10)	< -16	5.715(11)
004312.7+410531.5	17.5	-5.0505(59)	-2.1345(59)	-1.156(104)	-0.245(15)	-14.654(217)	5.535(17)
004313.2+410632.4	16.7	-4.9888(51)	-2.0494(49)	-0.917(60)	-0.245(15)	-13.857(32)	5.581(16)
004314.0+413906.3	17.7	-4.8902(40)	-1.9480(39)	-0.851(51)	-0.057(10)	-13.379(31)	5.740(11)
004315.2+414947.4	...	-5.1282(70)	-2.1967(68)	< -1.3	-1.106(111)	< -16	...
004317.9+410252.8	18.0	-4.9071(42)	-1.9826(42)	-1.066(84)	-0.785(53)	-14.241(78)	5.232(35)
004320.1+410611.1	16.7	-5.0353(57)	-2.0934(54)	-1.071(85)	-0.241(15)	< -16	5.554(17)
004320.8+414038.5	16.7	-5.1058(66)	-2.1748(65)	-0.828(49)	-0.168(13)	-13.559(31)	5.646(13)
004321.7+414033.2	16.7	-4.9135(43)	-1.9972(43)	-0.829(49)	-0.169(13)	-14.910(220)	5.657(13)
004322.0+414116.5	18.0	-5.0447(58)	-2.1110(56)	-0.979(69)	-0.266(16)	-14.131(109)	5.548(17)
004324.1+414124.7	17.7	-4.7677(31)	-1.8498(31)	-0.908(59)	-0.272(16)	< -16	5.586(15)
004324.3+414418.7	16.0	-4.9325(45)	-1.9896(42)	< -1.3	-0.683(42)	< -16	...
004324.4+410802.9	18.2	-4.9192(43)	-1.9663(40)	-0.890(56)	-0.228(15)	-13.726(32)	5.606(15)
004326.4+410508.4	15.5	-4.9428(46)	-2.0064(44)	-0.813(47)	-0.627(37)	-13.320(12)	5.390(25)
004328.2+414122.1	16.5	-5.3977(130)	-2.4545(124)	-1.226(122)	-0.683(42)	-13.666(109)	5.174(41)
004328.6+411818.0	18.4	-5.1019(66)	-2.1886(67)	< -1.3	-0.420(23)	< -16	...
004330.4+412757.0	18.6	-5.1139(68)	-2.2057(70)	< -1.3	< -1.2	< -16	...
004330.4+414432.5	17.0	-5.1580(75)	-2.2254(73)	< -1.3	-0.728(46)	< -16	...
004331.2+414222.9	18.7	-5.1305(70)	-2.1888(67)	-0.975(68)	-0.025(9)	-13.719(78)	5.734(11)
004331.3+414243.6	17.2	-4.9259(44)	-1.9962(43)	-0.847(51)	-0.023(9)	-13.928(105)	5.763(10)
004332.1+414251.8	17.2	-4.9215(43)	-1.9962(43)	-0.845(51)	-0.025(9)	-13.710(78)	5.762(10)
004332.4+414227.5	18.7	-4.9212(43)	-1.9905(42)	-0.939(63)	-0.025(9)	-13.556(55)	5.749(10)
004333.6+411432.3	18.4	-5.0642(60)	-2.1010(55)	< -1.3	-0.462(25)	< -16	...
004334.9+410953.6	22.1	-3.9057(4)	-1.0346(5)	0.040(7)	0.316(4)	-11.987(1)	6.304(3)
004338.7+411222.1	19.4	-4.8841(40)	-1.9527(39)	-0.697(36)	-0.128(12)	-13.367(28)	5.719(11)
004339.1+411018.4	18.5	-4.6475(23)	-2.0628(50)	-0.796(45)	-0.174(13)	-13.206(20)	5.655(13)
004339.3+411001.1	18.9	-4.6443(23)	-2.0469(48)	-0.729(39)	-0.165(13)	-14.068(44)	5.678(12)
004339.7+414534.9	16.2	-4.9414(46)	-2.0344(47)	< -1.3	0.048(8)	-13.821(93)	...
004340.8+411152.7	19.2	-5.0530(59)	-2.1398(60)	-1.024(76)	-0.137(12)	-14.073(103)	5.639(14)
004341.6+411135.3	19.2	-4.8314(35)	-1.9202(36)	-0.859(52)	-0.109(11)	-14.380(150)	5.702(12)
004341.7+412302.9	19.4	-4.8575(38)	-2.1461(61)	-0.957(66)	-0.323(18)	-13.115(20)	5.509(19)
004341.7+414519.4	20.3	-4.5516(19)	-1.6059(18)	-0.420(19)	0.039(8)	-13.827(55)	5.931(7)
004343.4+414521.6	15.8	-4.8657(38)	-1.9276(37)	-0.421(19)	0.038(8)	-13.801(23)	5.905(7)
004344.6+412321.3	17.8	-4.9697(49)	-2.0954(54)	-1.058(83)	-0.414(23)	-13.457(24)	5.430(22)
004346.3+414418.5	16.3	-4.8921(41)	-1.9650(40)	-0.972(68)	-0.307(18)	-14.391(148)	5.535(17)
004346.8+411239.7	19.1	-4.3525(12)	-1.6626(20)	-0.590(28)	-0.044(10)	-13.003(15)	5.828(9)
004348.1+411133.2	19.1	-4.4973(16)	-1.5627(16)	-0.470(21)	0.035(8)	-13.595(26)	5.920(7)
004349.0+415657.7	...	-5.2094(84)	-2.4394(119)	< -1.3	-1.056(99)	-14.255(152)	...
004349.4+411053.8	18.6	-4.8635(38)	-1.9029(35)	-0.968(67)	-0.605(35)	< -16	5.366(26)

Table 3 *continued*

Table 3 (*continued*)

Object (J2000)	T_{dust} (K)	$\log(\text{SFR})$ ($M_{\odot} \text{ yr}^{-1}$)	$\log(24 \mu\text{m})$ (Jy)	$\log(70 \mu\text{m})$ (Jy)	$\log(160 \mu\text{m})$ (Jy)	$\log(\text{H}\alpha)$ (mW m^{-2})	$\log(L_{\text{TIR}})$ (L_{\odot})
004351.4+414706.2	15.1	-5.1971(82)	-2.4053(110)	< -1.3	-0.527(29)	< -16	...
004351.4+415718.7	22.8	-5.0053(53)	-2.3631(100)	-1.063(84)	-0.802(55)	-14.310(35)	5.163(42)
004352.5+412524.1	17.9	-4.8094(34)	-1.8558(31)	-0.819(48)	-0.035(9)	-14.580(82)	5.769(10)
004352.5+414858.8	18.6	-5.0782(62)	-2.1668(64)	< -1.3	0.182(6)	< -16	...
004353.9+415743.8	24.8	-4.4913(16)	-1.7087(22)	-0.609(29)	-0.358(20)	-12.870(3)	5.639(14)
004354.8+414715.6	17.6	-4.7009(26)	-1.9636(40)	< -1.3	-0.456(25)	-13.699(74)	...
004354.9+412603.6	19.1	-4.7401(29)	-1.7926(27)	-0.673(34)	-0.078(10)	-13.187(7)	5.773(10)
004355.1+411433.1	18.2	-5.1765(78)	-2.2579(79)	-1.235(124)	-0.575(33)	-14.381(77)	5.265(33)
004355.2+412650.8	18.7	-4.9250(44)	-1.9728(41)	-0.821(48)	-0.091(11)	-13.796(17)	5.717(11)
004356.6+412629.6	18.7	-4.2253(9)	-1.2929(9)	-0.223(12)	0.264(5)	-12.680(3)	6.159(4)
004356.8+414831.6	20.1	-4.2654(10)	-1.3381(9)	-0.224(12)	0.171(6)	-12.947(16)	6.097(4)
004357.7+414854.0	19.9	-4.4812(16)	-1.5624(16)	-0.598(29)	-0.152(12)	-13.298(39)	5.775(10)
004358.2+414726.9	19.6	-4.8496(37)	-1.9039(35)	-0.919(60)	-0.333(19)	-13.417(40)	5.536(17)
004358.7+414837.5	20.0	-4.5883(20)	-1.6625(20)	-0.690(35)	0.171(6)	-13.697(64)	5.963(6)
004358.9+411742.1	19.2	-4.8941(41)	-2.0180(45)	-0.930(62)	-0.182(13)	-14.193(90)	5.627(14)
004401.5+414909.6	20.0	-3.2491(1)	-0.3130(1)	0.596(2)	0.686(2)	-12.514(4)	6.818(0)
004403.0+414954.7	18.9	-4.4677(15)	-1.5211(14)	-0.590(28)	-0.121(11)	-13.245(23)	5.802(9)
004403.4+411708.2	18.6	-4.9811(50)	-2.0621(50)	-0.904(58)	-0.123(12)	-13.281(18)	5.672(13)
004404.2+412107.8	18.1	-5.0524(59)	-2.1421(60)	-1.026(77)	-0.341(19)	-13.893(22)	5.483(20)
004404.9+415016.1	18.9	-4.9472(46)	-2.0092(44)	-1.099(91)	-0.115(11)	< -16	5.656(13)
004405.2+412718.2	18.2	-4.8902(40)	-2.0492(49)	-0.851(51)	-0.195(14)	-13.310(10)	5.630(14)
004405.7+411719.7	18.5	-5.3148(108)	-2.3050(88)	-0.904(58)	-0.327(18)	< -16	5.507(19)
004406.4+412745.0	17.9	-4.6878(25)	-1.7748(26)	-0.996(72)	-0.112(11)	-14.873(104)	5.695(12)
004407.0+412759.3	17.1	-4.6618(24)	-1.7509(24)	-0.803(46)	-0.110(11)	-13.319(10)	5.729(11)
004407.8+412110.7	18.0	-4.7292(28)	-1.8443(30)	-0.765(42)	-0.093(11)	-13.182(5)	5.737(11)
004409.2+413331.9	19.5	-4.9933(51)	-2.0750(52)	-1.093(90)	0.160(6)	-13.342(26)	5.888(7)
004410.6+411653.4	17.7	-5.2515(93)	-2.2459(77)	-1.282(138)	-0.334(19)	< -16	5.440(22)
004411.0+413206.3	19.0	-4.4552(15)	-1.9560(39)	-0.706(37)	-0.291(17)	-13.294(12)	5.611(15)
004411.8+414747.5	20.1	-5.1894(81)	-2.4230(115)	< -1.3	-0.691(43)	< -16	...
004411.9+413356.4	18.7	-4.8356(36)	-1.9150(36)	-0.832(49)	-0.050(10)	-13.338(18)	5.751(10)
004412.1+413320.5	19.5	-4.4494(15)	-1.5412(15)	-0.374(17)	0.159(6)	-13.747(4)	6.026(5)
004413.7+413413.5	17.8	-4.8900(40)	-1.9563(39)	-1.049(81)	0.010(8)	-14.542(166)	5.768(10)
004414.4+411742.3	18.0	-5.0980(65)	-2.3253(92)	< -1.3	-0.374(21)	< -16	...
004414.6+412840.3	17.2	-5.1261(70)	-2.2180(72)	< -1.3	-0.341(19)	-14.991(90)	...
004415.3+411905.7	19.6	-4.7348(28)	-1.8772(33)	-0.936(62)	-0.224(15)	< -16	5.610(15)
004415.9+411717.6	18.0	-4.9852(50)	-2.0706(51)	-0.943(63)	-0.223(15)	-13.733(56)	5.590(15)
004416.0+414950.7	18.1	-5.0169(54)	-2.1418(60)	-1.124(96)	-0.588(34)	< -16	5.294(31)
004416.1+412105.4	17.2	-4.6062(21)	-2.0480(49)	-0.811(47)	-0.067(10)	-13.424(8)	5.732(11)
004416.3+411730.9	18.0	-4.9705(49)	-2.0618(50)	-0.947(64)	-0.224(15)	-13.921(65)	5.589(15)
004416.7+412444.1	19.0	-5.2541(94)	-2.3265(92)	< -1.3	-0.626(37)	< -16	...
004418.2+413406.6	18.7	-4.6939(26)	-1.8145(28)	-0.615(30)	-0.247(15)	-13.745(55)	5.680(12)
004419.2+411930.9	19.1	-4.9306(44)	-2.0346(47)	-0.927(61)	-0.252(16)	< -16	5.575(16)
004419.3+412247.0	18.2	-5.0653(61)	-2.2134(71)	-0.851(51)	-0.606(35)	-13.429(5)	5.360(26)
004419.9+412201.2	18.8	-5.0387(57)	-2.0345(47)	-1.071(85)	-0.421(23)	< -16	5.429(22)
004420.2+415101.5	18.7	-4.8108(34)	-1.8905(34)	-0.841(50)	-0.112(11)	-13.747(126)	5.705(12)
004420.7+411751.0	18.9	-4.7490(29)	-2.0898(53)	-1.048(81)	-0.347(19)	-12.932(6)	5.479(20)
004420.9+411835.7	17.9	-4.9997(52)	-2.1416(60)	-1.040(79)	-0.353(20)	< -16	5.471(20)
004422.8+412529.1	16.5	-5.1825(79)	-2.2573(79)	< -1.3	-0.213(14)	< -16	...
004423.0+412050.9	21.8	-4.7372(28)	-1.8108(28)	-0.599(29)	0.080(7)	-13.757(10)	5.898(7)
004423.3+413842.6	16.5	-4.5496(18)	-1.6419(19)	-0.659(33)	-0.038(9)	-13.757(43)	5.819(9)

Table 3 *continued*

Table 3 (*continued*)

Object (J2000)	T_{dust} (K)	$\log(\text{SFR})$ ($M_{\odot} \text{ yr}^{-1}$)	$\log(24 \mu\text{m})$ (Jy)	$\log(70 \mu\text{m})$ (Jy)	$\log(160 \mu\text{m})$ (Jy)	$\log(\text{H}\alpha)$ (mW m^{-2})	$\log(L_{\text{TIR}})$ (L_{\odot})
004423.7+412437.3	17.8	-4.6880(25)	-1.7664(25)	-0.766(42)	-0.209(14)	-13.582(8)	5.669(13)
004424.1+412117.3	19.2	-4.7748(31)	-1.8520(31)	-0.631(31)	0.044(8)	-13.507(10)	5.862(8)
004424.2+414918.9	18.0	-4.3943(13)	-1.4720(13)	-0.413(19)	0.226(5)	-13.077(37)	6.069(5)
004424.4+415120.5	18.2	-5.0110(53)	-2.0776(52)	-1.007(74)	0.080(7)	< -16	5.825(9)
004424.9+413739.1	17.1	-4.5774(20)	-1.6303(19)	-0.632(31)	0.092(7)	-13.654(18)	5.916(7)
004425.0+414942.6	17.2	-4.6975(26)	-1.7512(24)	-0.580(27)	0.226(5)	-13.338(59)	6.015(5)
004425.4+415006.1	17.4	-4.9940(51)	-2.1067(56)	-0.923(61)	0.226(5)	-12.963(40)	5.959(6)
004426.2+412054.1	19.2	-4.3132(11)	-1.7607(25)	-0.499(23)	0.079(7)	-13.492(12)	5.922(7)
004426.7+412729.3	17.2	-4.7260(28)	-1.7936(27)	-0.726(39)	-0.310(18)	-15.166(134)	5.614(14)
004427.5+413529.8	17.2	-4.7609(30)	-1.8385(30)	-0.846(51)	-0.512(28)	-14.012(46)	5.462(21)
004429.1+412334.0	18.1	-4.7773(31)	-1.8833(33)	-1.036(79)	-0.217(14)	-13.815(38)	5.598(15)
004429.6+412138.9	18.7	-5.0040(53)	-2.0987(55)	-1.004(73)	-0.253(16)	-13.866(95)	5.555(17)
004429.6+415133.5	20.9	-4.7172(27)	-1.8366(30)	-0.666(34)	0.361(4)	-13.539(20)	6.110(4)
004430.2+415242.7	19.6	-4.8515(37)	-1.9999(43)	-0.839(50)	-0.120(11)	-14.377(30)	5.691(12)
004431.1+415110.2	19.7	-4.3936(13)	-1.4651(13)	-0.432(20)	-0.043(10)	-13.179(70)	5.898(7)
004431.1+415638.2	15.4	-4.9035(42)	-1.9894(42)	-0.917(60)	-0.293(17)	-13.415(46)	5.553(17)
004431.9+412233.3	17.5	-4.6621(24)	-1.7301(23)	-0.753(41)	-0.210(14)	-13.810(43)	5.676(12)
004431.9+412400.1	18.1	-4.5004(16)	-1.5924(17)	-0.740(40)	-0.019(9)	-13.061(18)	5.824(9)
004432.6+412518.7	18.3	-4.7475(29)	-2.1212(57)	-0.830(49)	-0.106(11)	-12.917(11)	5.695(12)
004436.7+412445.1	21.2	-4.6957(26)	-1.8717(32)	-0.702(36)	-0.059(10)	-13.291(12)	5.772(10)
004437.3+415350.2	17.5	-5.1285(70)	-2.2689(81)	< -1.3	-0.624(37)	< -16	...
004437.7+415259.8	18.4	-4.8410(36)	-2.2114(71)	-1.004(73)	-0.312(18)	-12.870(5)	5.502(19)
004437.9+415154.0	19.0	-3.9319(4)	-0.9921(4)	0.117(6)	0.319(4)	-12.936(5)	6.340(2)
004438.5+412511.1	21.2	-3.8788(4)	-0.9531(4)	0.063(6)	0.309(4)	-12.395(2)	6.324(2)
004439.4+415251.3	17.7	-4.8976(41)	-2.0451(48)	-1.046(80)	-0.303(17)	-14.114(43)	5.516(18)
004440.3+414923.9	15.6	-5.0228(55)	-2.0880(53)	-1.064(84)	-1.053(98)	< -16	5.102(48)
004441.5+415312.7	17.4	-5.0769(62)	-2.2386(75)	-1.072(86)	-0.279(17)	-13.642(23)	5.513(18)
004441.7+412659.6	18.3	-4.7707(31)	-1.9359(37)	-0.712(37)	0.087(7)	-13.936(21)	5.874(8)
004442.7+415341.1	20.8	-4.9439(46)	-2.1163(57)	< -1.3	-0.452(25)	< -16	...
004443.9+412758.0	19.0	-4.3710(12)	-1.4548(12)	-0.288(14)	0.337(4)	-13.924(56)	6.174(4)
004444.1+415359.0	17.2	-4.3236(11)	-1.4036(11)	-0.532(25)	-0.155(12)	-13.144(7)	5.822(9)
004444.8+412839.9	17.7	-4.8181(34)	-1.9487(39)	-0.898(57)	-0.190(13)	-13.380(30)	5.633(14)
004447.1+415657.7	17.2	-4.9431(46)	-2.1980(69)	-1.081(87)	-0.865(64)	-13.020(18)	5.148(43)
004447.6+412641.5	17.9	-4.9510(47)	-2.0890(53)	-0.956(65)	-0.205(14)	-13.375(37)	5.600(15)
004448.1+415307.3	17.0	-5.2305(89)	-2.3184(90)	< -1.3	-0.404(22)	< -16	...
004448.4+412254.2	20.9	-4.3531(12)	-1.4353(12)	-0.800(46)	-0.659(40)	-13.845(24)	5.530(18)
004448.6+415343.6	17.0	-5.1031(66)	-2.1271(58)	-1.041(80)	-0.144(12)	< -16	5.631(14)
004450.6+415608.3	15.9	-5.3124(107)	-2.3873(106)	-1.176(108)	-0.630(37)	-14.179(27)	5.228(36)
004450.9+412909.2	19.1	-4.2998(10)	-2.0339(47)	-0.842(50)	-0.200(14)	-13.721(26)	5.629(14)
004451.8+415423.7	17.5	-5.1995(83)	-2.3176(90)	-1.165(106)	-0.438(24)	-13.249(8)	5.371(26)
004452.7+415309.1	16.7	-4.9929(51)	-2.0353(47)	-0.958(66)	-0.304(17)	-13.290(12)	5.532(18)
004452.8+415457.5	17.7	-5.0343(56)	-2.1129(56)	-1.151(102)	-0.237(15)	-13.625(13)	5.544(17)
004453.0+415340.3	16.8	-4.6765(25)	-1.7310(23)	-0.753(41)	-0.046(10)	-13.854(27)	5.785(10)
004454.4+420327.4	19.4	-5.0722(62)	-2.1349(59)	-0.877(55)	-0.801(55)	< -16	5.268(33)
004456.1+412918.2	19.6	-4.4831(16)	-1.5448(15)	-0.398(18)	0.098(7)	-13.932(23)	5.980(6)
004456.2+413124.1	19.0	-4.3614(12)	-1.7588(25)	-0.558(26)	0.146(6)	-12.767(7)	5.957(6)
004457.2+415524.0	18.9	-4.5763(20)	-1.6597(20)	-0.591(28)	0.028(8)	-13.599(11)	5.876(8)
004457.3+413141.8	19.0	-4.4661(15)	-1.7166(23)	-0.518(24)	0.147(6)	-12.686(9)	5.969(6)
004458.0+414034.7	16.7	-5.1457(73)	-2.2305(74)	-1.157(104)	-0.581(33)	-13.754(22)	5.281(32)
004458.1+420008.6	15.4	-5.2691(97)	-2.3310(93)	< -1.3	-1.016(90)	-14.462(149)	...

Table 3 *continued*

Table 3 (*continued*)

Object (J2000)	T_{dust} (K)	$\log(\text{SFR})$ ($M_{\odot} \text{ yr}^{-1}$)	$\log(24 \mu\text{m})$ (Jy)	$\log(70 \mu\text{m})$ (Jy)	$\log(160 \mu\text{m})$ (Jy)	$\log(\text{H}\alpha)$ (mW m^{-2})	$\log(L_{\text{TIR}})$ (L_{\odot})
004458.3+415906.9	17.8	-5.2404(91)	-2.3273(92)	< -1.3	-0.843(61)	-13.886(81)	...
004458.7+415536.1	18.9	-4.3969(13)	-1.5519(15)	-0.598(29)	0.027(8)	-12.943(3)	5.887(7)
004459.1+413233.8	18.6	-4.3414(11)	-1.4118(11)	-0.329(15)	0.011(8)	-13.281(16)	5.967(6)
004459.1+414058.5	15.6	-4.1600(8)	-1.2325(7)	< -1.3	-1.009(89)	< -16	...
004459.3+413139.2	20.0	-4.4452(15)	-1.5399(15)	-0.359(17)	0.191(6)	-14.406(90)	6.051(5)
004459.5+415510.4	16.9	-4.9471(46)	-2.0166(45)	-0.957(66)	-0.085(11)	-13.513(11)	5.697(12)
004500.7+412836.9	21.2	-4.0326(6)	-1.0984(5)	-0.054(8)	0.104(7)	-12.914(10)	6.162(4)
004500.9+413101.1	18.9	-4.3028(10)	-1.4258(12)	-0.305(15)	0.121(7)	-12.642(7)	6.033(5)
004503.0+413249.4	17.7	-4.9860(50)	-2.1026(55)	-1.005(73)	-0.104(11)	-14.996(36)	5.670(13)
004504.6+413237.6	16.8	-5.1813(79)	-2.3970(108)	-1.279(138)	-0.100(11)	< -16	5.631(14)
004505.3+413845.9	16.6	-5.0585(60)	-2.2161(71)	-1.153(103)	-0.265(16)	-14.471(10)	5.514(18)
004505.9+413925.5	17.2	-5.1266(70)	-2.1741(65)	-1.259(132)	-0.280(17)	-13.474(5)	5.492(19)
004506.1+413615.0	19.0	-4.5365(18)	-1.6168(18)	-0.731(39)	-0.227(15)	< -16	5.689(12)
004506.1+415121.0	16.0	-4.6948(26)	-1.7539(25)	-0.608(29)	0.019(8)	-13.714(16)	5.856(8)
004506.2+413424.4	19.0	-4.4196(14)	-1.5000(14)	-0.337(16)	0.176(6)	-12.932(10)	6.050(5)
004506.9+413407.8	17.6	-4.3522(12)	-1.4338(12)	-0.333(16)	0.169(6)	-13.547(5)	6.054(5)
004507.5+413439.4	18.3	-4.8158(34)	-1.8864(33)	-0.839(50)	0.061(8)	-13.947(10)	5.838(8)
004508.2+413424.2	18.3	-4.6107(21)	-1.6692(20)	-0.679(35)	0.065(7)	-13.936(7)	5.884(8)
004509.0+415209.7	16.1	-5.0343(56)	-2.0894(53)	-0.955(65)	-0.276(16)	< -16	5.547(17)
004510.0+420143.6	20.2	-5.2208(87)	-2.3545(98)	-1.281(138)	-0.670(41)	-13.686(33)	5.180(40)
004510.3+420228.5	19.8	-5.0824(63)	-2.1822(66)	-1.044(80)	-0.698(43)	-13.278(16)	5.247(34)
004510.4+413716.0	21.3	-3.9140(4)	-1.0083(4)	0.043(7)	0.381(4)	-13.034(4)	6.343(2)
004510.5+413426.7	16.4	-4.9489(46)	-2.0121(45)	-1.052(82)	0.064(7)	-13.350(3)	5.811(9)
004510.8+415938.9	19.2	-5.1794(79)	-2.2579(79)	-1.171(107)	-0.843(61)	< -16	5.118(46)
004511.2+413644.9	18.6	-4.5988(21)	-1.7915(27)	-0.787(44)	0.384(4)	-13.335(4)	6.121(4)
004511.3+413633.9	18.6	-4.7385(29)	-1.8369(30)	-0.869(54)	0.388(4)	< -16	6.116(4)
004511.6+420130.3	20.2	-5.1146(68)	-2.1812(66)	-1.027(77)	-0.725(46)	-14.585(32)	5.238(35)
004512.1+415542.5	16.1	-5.1369(71)	-2.1982(69)	-1.014(75)	-0.200(14)	< -16	5.586(15)
004512.4+413709.6	21.3	-3.9130(4)	-1.0074(4)	0.043(7)	0.385(4)	-12.996(1)	6.345(2)
004512.8+413531.6	18.2	-4.2568(9)	-1.3140(9)	-0.291(14)	0.105(7)	-13.959(11)	6.045(5)
004514.4+413723.6	20.1	-4.8652(38)	-1.9749(41)	-0.801(46)	0.386(4)	-13.054(2)	6.114(4)
004515.2+413948.5	17.1	-5.0315(56)	-2.1022(55)	< -1.3	-0.028(9)	< -16	...
004518.1+413920.5	18.4	-4.5784(20)	-1.9751(41)	-0.875(54)	-0.026(9)	-13.189(1)	5.759(10)
004518.5+414013.2	18.1	-4.6856(25)	-1.8179(29)	-0.769(43)	-0.175(13)	-13.004(13)	5.683(12)
004518.7+413906.1	17.9	-4.8485(37)	-1.9704(41)	-0.899(57)	-0.060(10)	-13.062(2)	5.728(11)
004518.8+420331.8	16.8	-5.0582(60)	-2.1253(58)	-1.138(100)	-0.581(33)	< -16	5.298(30)
004520.7+414716.7	16.4	-4.7290(28)	-1.7296(23)	-1.013(75)	-0.512(28)	-14.642(28)	5.442(22)
004520.9+414248.8	17.4	-5.3302(111)	-2.3578(99)	-1.211(118)	-0.433(24)	-14.735(35)	5.364(26)
004521.6+420345.1	17.0	-5.0361(57)	-2.0943(54)	-1.102(92)	-0.376(21)	< -16	5.448(21)
004523.1+414346.0	18.8	-5.1902(81)	-2.2886(84)	< -1.3	-0.342(19)	-13.896(8)	...
004524.4+415537.4	17.2	-4.5744(20)	-1.6410(19)	-0.672(34)	-0.368(20)	-15.279(43)	5.626(14)
004526.8+415820.1	17.1	-5.2940(103)	-2.3249(92)	< -1.3	-0.693(43)	-13.580(10)	...
004527.0+415135.5	16.3	-5.3824(126)	-2.4036(110)	< -1.3	-0.633(37)	< -16	...
004528.0+415928.1	18.2	-5.2052(84)	-2.3099(89)	-1.211(118)	-0.763(50)	-14.269(21)	5.143(44)
004528.2+414513.6	19.4	-4.5514(19)	-1.6125(18)	-0.691(36)	-0.090(11)	-14.085(20)	5.783(10)
004528.2+414630.6	19.3	-5.0728(62)	-2.1433(60)	-1.063(84)	-0.215(14)	-13.710(6)	5.571(16)
004528.6+415000.2	18.2	-4.8639(38)	-2.2080(70)	-0.985(70)	-0.224(15)	-12.827(2)	5.572(16)
004532.2+414543.3	17.1	-5.0694(61)	-2.1857(67)	-1.117(95)	-0.309(18)	-14.886(60)	5.487(20)
004533.3+414739.8	19.1	-4.8782(39)	-2.0410(48)	-0.756(41)	-0.136(12)	-13.229(5)	5.693(12)
004533.6+414728.2	19.3	-4.8787(39)	-2.0595(50)	-0.768(42)	-0.136(12)	-14.111(19)	5.689(12)

Table 3 *continued*

Table 3 (*continued*)

Object (J2000)	T _{dust} (K)	log(SFR) (M _⊙ yr ⁻¹)	log(24 μm) (Jy)	log(70 μm) (Jy)	log(160 μm) (Jy)	log(Hα) (mW m ⁻²)	log(L _{TIR}) (L _⊙)
004534.1+414703.3	19.3	-4.9134(43)	-2.1692(64)	-0.826(48)	-0.135(12)	< -16	5.671(13)
004536.3+414252.0	19.6	-4.9490(46)	-2.0356(47)	-0.920(60)	-0.228(15)	-13.788(133)	5.593(15)
004536.5+415307.7	15.0	-5.0280(56)	-2.0748(52)	-0.878(55)	-0.184(13)	-14.162(11)	5.630(14)
004536.9+415704.0	17.8	-5.0349(56)	-2.1346(59)	-1.131(98)	-0.534(30)	-13.517(8)	5.329(28)
004537.2+415802.4	17.9	-4.8658(38)	-1.9364(38)	-0.921(60)	-0.420(23)	-13.991(25)	5.476(20)
004537.3+415107.0	18.0	-4.5484(18)	-1.6462(19)	-0.521(24)	-0.113(11)	-13.002(1)	5.806(9)
004537.6+415424.1	16.9	-4.9037(42)	-1.9941(43)	-0.902(58)	-0.226(15)	-13.979(6)	5.602(15)
004538.5+415231.1	19.0	-4.9639(48)	-2.0738(51)	-0.895(57)	-0.283(17)	-13.357(4)	5.557(17)
004541.4+415550.4	17.1	-4.8869(40)	-2.0372(47)	-0.931(62)	-0.103(11)	-13.198(9)	5.685(12)
004541.6+415107.7	17.5	-4.6032(21)	-1.6729(20)	-0.660(33)	-0.178(13)	< -16	5.727(11)
004542.9+415234.8	19.3	-4.6572(24)	-1.7338(24)	-0.687(35)	-0.193(14)	-13.775(6)	5.702(12)
004543.3+415109.3	17.5	-5.0047(53)	-2.0974(54)	-1.070(85)	-0.169(13)	-13.788(8)	5.609(15)
004543.3+415301.1	19.0	-4.2528(9)	-1.3254(9)	-0.225(12)	0.070(7)	-12.654(1)	6.045(5)
004543.5+414235.1	20.1	-5.1210(69)	-2.2232(73)	-1.095(90)	-0.838(60)	-13.575(7)	5.152(43)
004544.3+415207.4	19.0	-4.2272(9)	-1.3060(9)	-0.401(18)	-0.061(10)	-13.303(2)	5.927(7)
004549.7+421017.1	21.1	-4.7933(32)	-1.8795(33)	-0.723(38)	-0.461(25)	-13.146(5)	5.522(18)
004555.2+415645.8	16.8	-4.5123(17)	-1.5822(17)	-0.472(21)	-0.482(26)	< -16	5.667(13)
004608.5+421131.0	20.6	-3.4461(1)	-0.5113(1)	0.103(6)	-0.020(9)	-13.527(6)	6.378(2)
004613.4+415224.4	17.0	-4.8755(39)	-2.2136(71)	-0.935(62)	-0.553(31)	-13.708(1)	5.360(26)
004617.6+415158.0	21.3	-4.1410(7)	-1.2141(7)	-0.357(16)	-0.461(25)	-13.688(1)	5.823(9)
004623.9+421215.2	17.2	-5.2879(101)	-2.4076(111)	-1.266(134)	-0.686(42)	< -16	5.167(41)
004625.4+421156.0	16.7	-5.0749(62)	-2.3725(102)	-1.252(129)	-0.745(48)	-13.544(13)	5.135(44)
004626.0+421121.7	17.5	-5.1991(82)	-2.4265(116)	< -1.3	-1.011(89)	-14.065(17)	...
004627.9+415920.4	20.7	-5.1533(74)	-2.2910(85)	-1.108(93)	-0.633(37)	-15.280(11)	5.253(34)
004631.5+421342.6	22.7	-4.9095(42)	-2.1422(60)	-0.949(64)	-0.402(22)	-12.910(3)	5.457(21)
004633.4+421244.2	19.7	-4.5140(17)	-2.1205(57)	-0.801(46)	-0.259(16)	-13.728(5)	5.591(15)
004633.6+415932.0	16.0	-4.7864(32)	-1.9623(40)	-1.179(109)	-0.566(32)	-13.955(18)	5.326(28)
004634.2+415636.8	17.5	-4.8480(37)	-1.9124(35)	-1.201(115)	-0.877(65)	-14.676(6)	5.170(41)
004634.4+421143.1	23.7	-3.7411(3)	-0.8991(3)	0.065(6)	0.227(5)	-12.337(1)	6.300(3)
004641.9+421547.8	17.1	-5.1089(67)	-2.3074(88)	-1.001(73)	-0.805(55)	-13.625(7)	5.191(39)
004642.2+415837.3	20.6	-5.2839(100)	-2.4016(109)	< -1.3	-0.966(80)	-14.987(73)	...
004645.9+420453.1	14.3	-4.9209(43)	-2.0005(43)	< -1.3	-1.054(98)	-15.268(93)	...
004654.5+420046.2	24.3	-5.0653(61)	-2.2576(79)	-1.212(118)	-0.877(66)	-13.914(2)	5.087(50)

NOTE—Table 3 is published in its entirety in the electronic edition of the *Astrophysical Journal*. A portion is shown here for guidance regarding its form and content. Parenthetical values indicate 1σ statistical uncertainties. The uncertainty in T_{dust} is 1.4 K (Smith et al. 2012). The 1σ uncertainties for photometric flux densities and SFR indicate statistical uncertainties for images with high signal to noise ratios, but the systematic uncertainties are likely to be higher.

3.3. Optical Counterparts

We cross-matched the GBT survey sample with the Azimlu et al. (2011) catalog of Hα flux-limited optically identified H II regions. We identified 346 Hα counterparts in the non-maser catalog using a positional uncertainty of 10". We also found four (out of five) Hα counterparts in the water maser sample. The Hα fluxes for the water maser and non-maser sources are listed in Table 2 and Table 3, respectively.

Not all objects in the GBT survey are H II regions, and not all H II regions in the survey are detected or measured in all properties used in the comparative analysis of maser- and non-maser-emitting regions. Here we present the process used to exclude planetary nebulae and giant stars from the sample (also excluded from the detection statistics presented in Darling et al. 2016), and we present the reduced study sample that has measurements of all quantities presented in Tables 2 and 3.

4. THE STUDY SAMPLE

4.1. Planetary Nebulae and Stellar Populations

Although star forming regions emit strong $24\ \mu\text{m}$ emission, they are not the only luminous $24\ \mu\text{m}$ sources in M31. There are sources which emit significant $24\ \mu\text{m}$ emission and are not associated with star forming regions, and these sources must be removed from the original sample of 506 sources.

Planetary Nebulae (PNe) can emit strong infrared radiation at $24\ \mu\text{m}$ and may represent a small fraction of the source sample. Merrett et al. (2006) present the results of a survey of 3300 emission line sources in M31 observed with the Planetary Nebulae Spectrograph. After removing the extended emission from HII regions and background galaxies, they identify 2615 PNe candidates in M31. We cross matched our source list with the catalog of PNe and identified nine PNe candidates in our sample and removed them from the rest of the analysis (Table 4).

The giant stellar populations in M31 can also produce significant $24\ \mu\text{m}$ emission. Red supergiants and asymptotic giant branch (AGB) stars show strong $3.4\ \mu\text{m}$ emission that originates in thick circumstellar shells (e.g. Barmby et al. 2006; Mould et al. 2008). In a recent study of dust heating in M31 using Herschel data in the wavelength range $70\text{--}500\ \mu\text{m}$, Groves et al. (2012) find that “old” stellar populations (of Gyr age) can emit significant infrared radiation. Ford et al. (2013) determine the effect of these stars on the apparent star formation rate from $24\ \mu\text{m}$ map by measuring the ratio of $\alpha = I_{24}/I_{3.4}$ in regions where there is no active star formation, where I_{24} and $I_{3.6}$ indicate the $24\ \mu\text{m}$ and $3.6\ \mu\text{m}$ intensity. They found significant correlation between $24\ \mu\text{m}$ and $3.6\ \mu\text{m}$ emission in the center of M31 predominantly from giant stars, and use $\alpha = 0.1$ to remove this component of the total $24\ \mu\text{m}$ emission.

We examine the association of our sample with stellar populations by comparing the flux density of the sample at $3.4\ \mu\text{m}$ to that at $22\ \mu\text{m}$. Aperture photometry was performed for the sources in the sample on the $3.4\ \mu\text{m}$ and $22\ \mu\text{m}$ WISE maps. We utilized the prescription for photometry described for WISE images in the user’s guide to the WISE Preliminary Data Release ⁶. We obtained uncertainties in flux densities by performing aperture photometry on 50 blank regions in each map and measuring the standard deviations in aperture photometric flux. The 3σ uncertainties at $3.4\ \mu\text{m}$ and $22\ \mu\text{m}$ are 0.16 and 0.18 mJy, respectively.

Figure 3 shows the $22\ \mu\text{m}$ vs. $3.4\ \mu\text{m}$ emission for the sample. The aperture radius of $5.5''$ was used to measure the flux density at 3.4 and $22\ \mu\text{m}$. We found that for 35 regions there is a clear separation from the rest

of the sample, suggesting that these are giant stars. We impose a $3.4\ \mu\text{m}$ cut at 0.03 Jy to separate giant stars from star-forming regions: giant stars form the more luminous population at $3.4\ \mu\text{m}$. Table 4 lists these 35 sources identified as giant stars, including their coordinates. We removed these giant stars from the sample, and after removing the nine PNe as well, the final source list includes 462 objects (five of which are maser sources) that are likely to be star-forming regions.

4.2. The Detection Sample

We construct a “detection” sample of 320 sources in the non-maser sample that have measured values for all properties for each object. The $24\ \mu\text{m}$ flux densities and SFR were measured for 457 non-maser sources. We measure flux densities at $70\ \mu\text{m}$ above 0.05 Jy (3σ) for 389 sources in the non-maser sample. At $160\ \mu\text{m}$ we obtain flux densities for 447 non-maser sources above 0.06 Jy (3σ). There are 346 H α counterparts for the non-maser sample. There are three sources in the non-maser sample with no temperature in the dust temperature map. The intersection of these sets includes 320 regions.

We measure all values for the water maser sample, except for the H α flux for the source 004409.4+411856.3. Since other properties for 004409.4+411856.3 were measured (Table 2), we include this source in the analysis. We only removed this object from the water maser sample where H α flux was involved in the statistics. This includes computing the correlation between H α and other variables and the Kolmogorov-Smirnov (K-S) test on H α in the maser and non-maser samples. Below we describe the results of statistical analyses we performed on the water masers and the “detection” sample of non-maser regions.

5. RESULTS

Figure 4 shows the distribution of the $24\ \mu\text{m}$, $70\ \mu\text{m}$, and $160\ \mu\text{m}$ flux densities, the H α flux, the dust temperature, and the star formation rate for the water maser hosts and the non-maser sources in the detection sample, and Figure 5 shows pairwise scatter plots in these quantities. All values used in the following analysis are tabulated in Tables 2 and 3.

6. ANALYSIS

The GBT water maser survey of 506 luminous compact $24\ \mu\text{m}$ regions produced five water maser detections. Sensitivity limitations of the observations (~ 10 mJy at 3σ) and imperfections in the selection criteria (44 objects were subsequently omitted as likely PNe or giant stars) aside, the low detection rate of 1.1(0.5)% (Darling et al. 2016) may indicate that water maser emission favors specific physical conditions in star forming regions in M31. To explore this possibility, we ex-

⁶ http://wise2.ipac.caltech.edu/docs/release/prelim/expsup/sec2_3f.html

Table 4. Planetary Nebulae and Giant Stars

Object (J2000)	Classification	Object (J2000)	Classification
003838.7+402613.5	Star	003849.2+402551.7	Star
003950.9+402252.1	PNe	003954.4+403820.4	Star
004040.4+402709.8	PNe	004129.8+412211.1	Star
004201.5+404115.7	Star	004208.9+412329.8	Star
004210.7+412322.3	Star	004226.1+410548.2	Star
004227.9+413258.5	Star	004228.1+405657.7	Star
004228.3+412911.4	Star	004228.4+412852.4	Star
004230.1+412904.0	Star	004230.9+405714.6	Star
004237.4+414158.3	Star	004241.7+411435.0	Star
004241.9+405155.2	Star	004242.6+411722.5	Star
004244.4+411608.5	Star	004245.3+411656.9	Star
004247.0+411618.4	Star	004248.2+411651.7	Star
004249.1+411554.6	Star	004249.1+411945.9	Star
004310.0+413751.6	PNe	004314.2+410033.9	Star
004325.6+410206.4	Star	004329.2+414848.0	PNe
004332.5+410907.0	Star	004339.4+412229.2	Star
004341.5+414224.3	Star	004341.7+415313.0	Star
004355.8+411211.6	PNe	004403.9+413414.8	Star
004410.5+420247.5	Star	004433.8+415249.7	PNe
004435.6+415606.9	PNe	004515.9+420254.4	Star
004540.0+415510.2	PNe	004641.6+421156.2	PNe
004642.6+421406.8	Star	004703.1+415755.4	Star

amine the optical, FIR, dust temperature, and star formation rate characteristics of the water maser and non-maser regions used in the GBT survey. Using two sample K-S tests, correlation statistics, principal component analysis, and survival analysis, we compare the properties of the water maser and non-maser samples. We then examine the FIR-H₂O maser luminosity relation and the role of star formation in the maser detection rate.

6.1. One-Parameter Tests

6.1.1. K-S Tests

We performed non-parametric two-sample K-S tests to examine the differences in properties of the water maser and non-maser regions. The p-values of these tests are listed in Table 5. The star formation rate and the 24 μm , 70 μm , and 160 μm flux densities have a p-value less than 0.05, suggesting significant differences between the maser-emitting regions and those that do not show maser emission. The dust temperature and H α emission do not show significant differences. Note that the maser sample is small, and that one of the masers, 004409.4+411856.3, is excluded from the H α statistic.

6.1.2. Survival Analysis

As discussed section 4.2, some values are listed as upper limits in Tables 2 and 3, and these objects were excluded from the “detection” sample analyzed above.

Alternatively, upper limits can be included in a survival analysis. We performed two-sample tests to study the difference between the measured (censored) properties of the water maser and non-maser regions using the survival analysis package Nondetections and Data Analysis for environmental data (NADA)⁷ implemented in R⁸. The NADA package has been shown to give results appropriate for astronomical data that includes non-detections (Feigelson & Babu 2013). We used the NADA “cendiff” routine and performed the Peto & Peto two-sample test, which is an appropriate treatment for left-censored data that include upper limits.

There are no dust temperatures for five sources in the non-maser sample, and since one cannot place upper limits on the dust temperature in these cases, these sources were omitted from the survival analysis. Table 6 shows the results of the two-sample test performed on the water maser and non-maser samples. The p-values indicate the probability that the two samples are drawn from the same distribution. The p-values for the dust temperature, the SFR, and the 24 μm , 70 μm , and 160 μm flux densities show that the water maser and

⁷ <http://cran.r-project.org/web/packages/NADA/NADA.pdf>

⁸ <https://www.R-project.org>

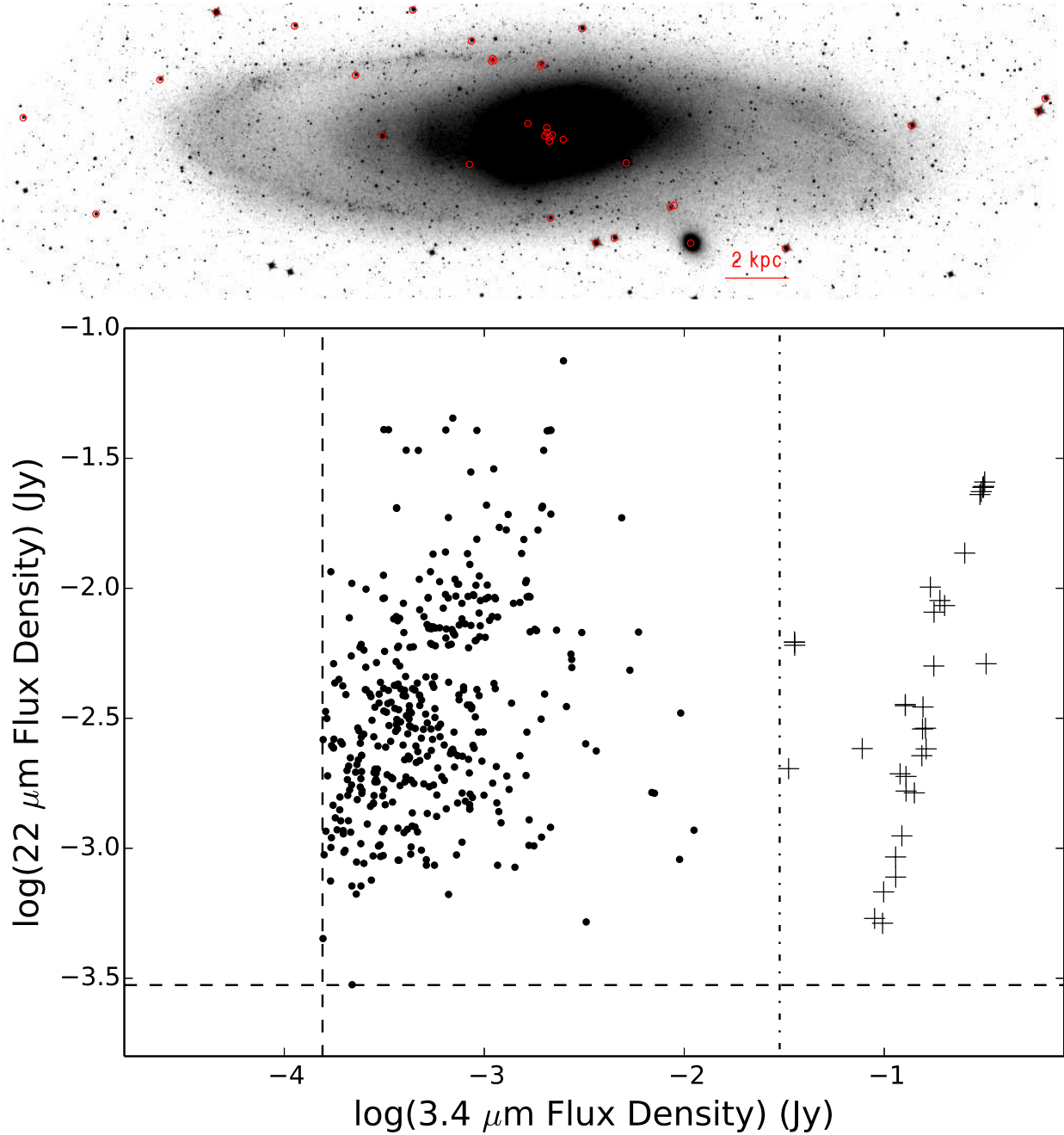


Figure 3. Identification of stellar interlopers in the star-forming regions sample. Upper panel: $3.4 \mu\text{m}$ WISE image of M31. The red circles show the giant star candidates identified in our sample. Plot: $22 \mu\text{m}$ vs. $3.4 \mu\text{m}$ flux density for the complete survey sample. Crosses indicate objects identified as giant stars, and filled circles indicate the rest of the sample. The dashed lines show the 3σ detection limit at $3.4 \mu\text{m}$ and the 5σ detection limit at $22 \mu\text{m}$. The vertical dashed-dotted line at 0.03 Jy separates the candidate giant stars from the rest of the sample.

Table 5. K-S Test of Water Maser Regions and Non-Maser Regions

	T_{dust}	$\log(\text{SFR})$	$\log(24 \mu\text{m})$	$\log(70 \mu\text{m})$	$\log(160 \mu\text{m})$	$\log(\text{H}\alpha)$
p-value	0.19	0.013	0.013	0.00075	0.041	0.11

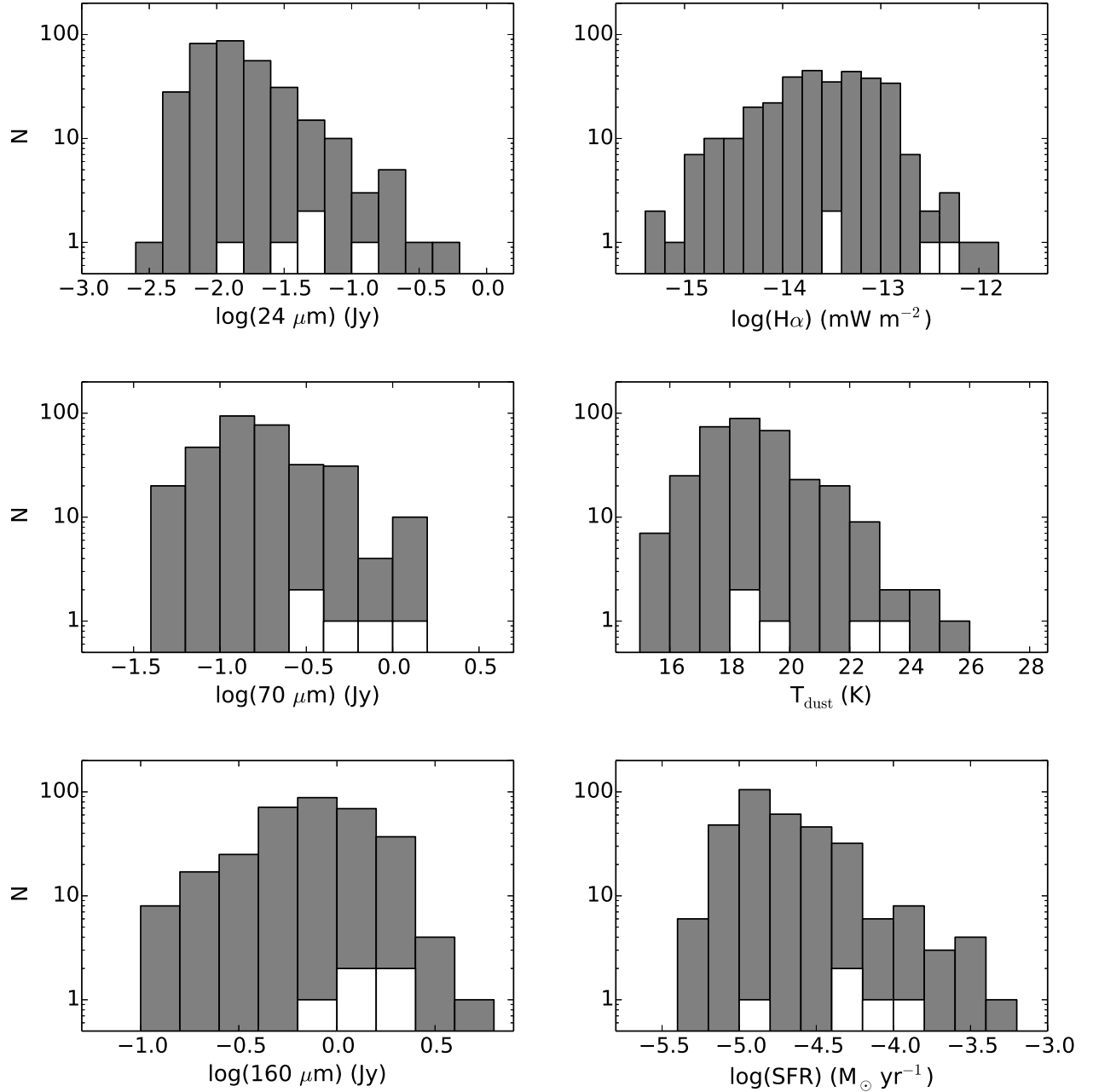


Figure 4. Distribution of the 24 μm , 70 μm , and 160 μm flux densities, the H α flux, the dust temperature, and the star formation rate for the water maser and non-maser objects. White bars show the water maser hosts and the black bars indicate the non-masers.

non-maser samples are not mutually consistent. The p-value for H α flux, however, indicates that the water maser and non-maser samples are indistinguishable. These results are similar to the K-S test results for the “detection” sample (Section 6.1.1) for the SFR and the 24 μm , 70 μm , and 160 μm flux densities, suggesting that the censorship on the samples did not significantly affect inferences made based only on the “detection” sample.

6.2. Two-Parameter Tests

We performed a correlation analysis of the properties of the water maser and non-maser regions separately. Table 7 lists the Pearson correlation coefficients for the water maser host properties, including the water maser line-integrated flux densities, and Table 8 lists the p-values associated with Pearson correlation coefficients (the probability that the correlation occurs by chance). Again, the H α flux of 004409.4+411856.3 is omitted from the analysis, but all other properties of this maser region are included.

Significant correlation exists between SFR, 24 μm , and 70 μm emission because these quantities are all driven by (or tautologically are) star formation. p-values are slightly larger than 0.05 for the correlations between SFR and other star formation-driven quantities, such as 160 μm and H α emission, most likely due to the very small sample size (see non-maser regions, below). Dust temperature also shows a significant correlation with H α . Water maser emission (flux) notably shows no significant correlation with any other measured property (but see Section 6.3), which is not surprising given the very small-scale emission regions of water masers that amplify local conditions. The bulk properties of star-forming regions, however, may still be predictive of the formation of water masers, even if one cannot predict the luminosity of the emitted masers (Section 6.4).

Table 9 lists the Pearson correlation coefficients for the non-maser sample, and Table 10 lists the associated p-values. All quantities are significantly correlated among the non-maser sample because all of the properties under study are related to star formation in the “detection” sample.

Figure 5 shows scatter plots of various pairs of properties for both maser and non-maser samples, focusing on those that show correlation in the water maser-emitting regions. The dashed-dotted lines indicate the regions of parameter space where masers are found, and where future surveys might concentrate. The loci are $\log(24\mu\text{m}) > -2.0$, $\log(70\mu\text{m}) > -0.6$, $\log(\text{SFR}) > -5.0$, and $\log(\text{H}\alpha) > -14.0$, in the units listed in Tables 2 and 3. The intersection of all of these limits reduces the sample to 70 sources, including four masers, yielding a detection rate of 5.7(2.8)%.

6.3. FIR-H $_2$ O Maser Luminosity Relation

Previous studies have shown that water masers in the Galaxy are associated with compact bright FIR sources. Jaffe et al. (1981) found that H $_2$ O maser emission in star-forming regions is associated with 50–100% of the bright Galactic FIR sources and that H $_2$ O maser luminosities are correlated with FIR luminosities. Felli et al. (1992) found a similar correlation between water maser luminosity and FIR luminosity in Galactic star-forming regions. Extragalactic water masers show a rough correlation between the water maser luminosity and FIR luminosity (Henkel et al. 2005; Castangia et al. 2008), although water megamasers and kilomasers appear to follow different correlations: for a given FIR luminosity, water kilomasers are sub-luminous compared to masers emitted from Galactic star-forming regions, and water megamasers appear to be slightly over-luminous.

Since the M31 water masers in principle represent analogs to the high end of the Galactic water maser luminosity distribution, it is useful to compare the FIR-H $_2$ O luminosity relation for water masers in M31 to Galactic and Extragalactic water masers. The infrared luminosity of star-forming regions in M31 can be calculated using Equation 4 in Dale & Helou (2002) that describes the total infrared (TIR) luminosities of galaxies in the range 3–1100 μm :

$$L_{TIR} = \zeta_1 \nu L_\nu(24 \mu\text{m}) + \zeta_2 \nu L_\nu(70 \mu\text{m}) + \zeta_3 \nu L_\nu(160 \mu\text{m}), \quad (1)$$

where $[\zeta_1, \zeta_2, \zeta_3] = [1.559, 0.7686, 1.347]$ for $z = 0$, and ν is the frequency in Hz. Dale & Helou (2002) explain that Equation 1 matches the model bolometric infrared luminosity to better than 1% at $z = 0$. It is therefore reasonable to assume that the TIR and bolometric luminosities of the water maser and non-maser samples can be obtained from Equation 1. We convert the flux density values at 24 μm , 70 μm , and 160 μm in Tables 2 and 3 to specific luminosities assuming a distance of 780 kpc ($L_\nu = 4\pi D^2 S_\nu$) and then calculate L_{TIR} . Tables 2 and 3 show the TIR luminosities for the maser and non-maser samples, respectively (for the non-maser sample, L_{TIR} is only calculated for the 387 sources that are detected in all three FIR bands). Figure 6 shows the distribution of the TIR luminosity of the water maser and non-maser sources in the M31 survey. Table 2 also lists the isotropic H $_2$ O maser luminosities obtained from Darling (2011).

Figure 7 shows the H $_2$ O-FIR (or -TIR) luminosity relation for Galactic and extragalactic water masers. The water masers in M31 are clearly consistent with the Galactic relation obtained by Jaffe et al. (1981) and overlap the high-luminosity tail of the Galactic distribution. This result suggests two things: (1) the M31 water masers do indeed seem to be analogs to the high-

Table 6. Survival Analysis of Water Maser and Non-Maser Regions

	T_{dust}	$\log(\text{SFR})$	$\log(24 \mu\text{m})$	$\log(70 \mu\text{m})$	$\log(160 \mu\text{m})$	$\log(\text{H}\alpha)$
p-value	0.0086	3.5×10^{-6}	3.6×10^{-7}	1.0×10^{-11}	4.2×10^{-5}	0.055

Table 7. Pearson Correlation Coefficients for the Water Maser-Emitting Regions in M31

	T_{dust}	$\log(\text{SFR})$	$\log(24 \mu\text{m})$	$\log(70 \mu\text{m})$	$\log(160 \mu\text{m})$	$\log(\text{H}\alpha)$	$\log(\text{H}_2\text{O})$
T_{dust}	1.00	0.78	0.76	0.82	0.36	0.96	0.54
$\log(\text{SFR})$		1.00	1.00	0.90	0.84	0.94	0.23
$\log(24 \mu\text{m})$			1.00	0.92	0.87	0.90	0.18
$\log(70 \mu\text{m})$				1.00	0.76	0.90	0.21
$\log(160 \mu\text{m})$					1.00	0.23	-0.19
$\log(\text{H}\alpha)$						1.00	0.46
$\log(\text{H}_2\text{O})$							1.00

Table 8. Pearson Correlation Coefficient p-values for the Water Maser-Emitting Regions

	T_{dust}	$\log(\text{SFR})$	$\log(24 \mu\text{m})$	$\log(70 \mu\text{m})$	$\log(160 \mu\text{m})$	$\log(\text{H}\alpha)$	$\log(\text{H}_2\text{O})$
T_{dust}		0.12	0.14	0.09	0.56	0.04	0.35
$\log(\text{SFR})$			0.00	0.04	0.07	0.06	0.71
$\log(24 \mu\text{m})$				0.03	0.05	0.10	0.77
$\log(70 \mu\text{m})$					0.13	0.10	0.73
$\log(160 \mu\text{m})$						0.77	0.76
$\log(\text{H}\alpha)$							0.54
$\log(\text{H}_2\text{O})$							

Table 9. Pearson Correlation Coefficients for the Non-Maser Sample in M31

	T_{dust}	$\log(\text{SFR})$	$\log(24 \mu\text{m})$	$\log(70 \mu\text{m})$	$\log(160 \mu\text{m})$	$\log(\text{H}\alpha)$
T_{dust}	1.00	0.42	0.37	0.43	0.15	0.29
$\log(\text{SFR})$		1.00	0.96	0.89	0.62	0.38
$\log(24 \mu\text{m})$			1.00	0.90	0.64	0.31
$\log(70 \mu\text{m})$				1.00	0.69	0.38
$\log(160 \mu\text{m})$					1.00	0.21
$\log(\text{H}\alpha)$						1.00

luminosity tail of the Galactic water maser distribution, suggesting that what is known about Galactic water masers can be applied to those in M31, and (2) a more sensitive survey of IR-luminous regions in M31 is likely to detect more water masers.

6.4. The Maser Detection Rate

The luminosity of the water masers in M31 seems to follow the same relationship with the FIR luminosity as do masers in the Galaxy and in other galaxies, but is the detection rate of water masers in line with the Galactic rate, scaled to the luminosity sensitivity of the GBT water maser survey?

In a survey of massive young stellar objects (MYSOs), compact HII regions, and ultra compact HII re-

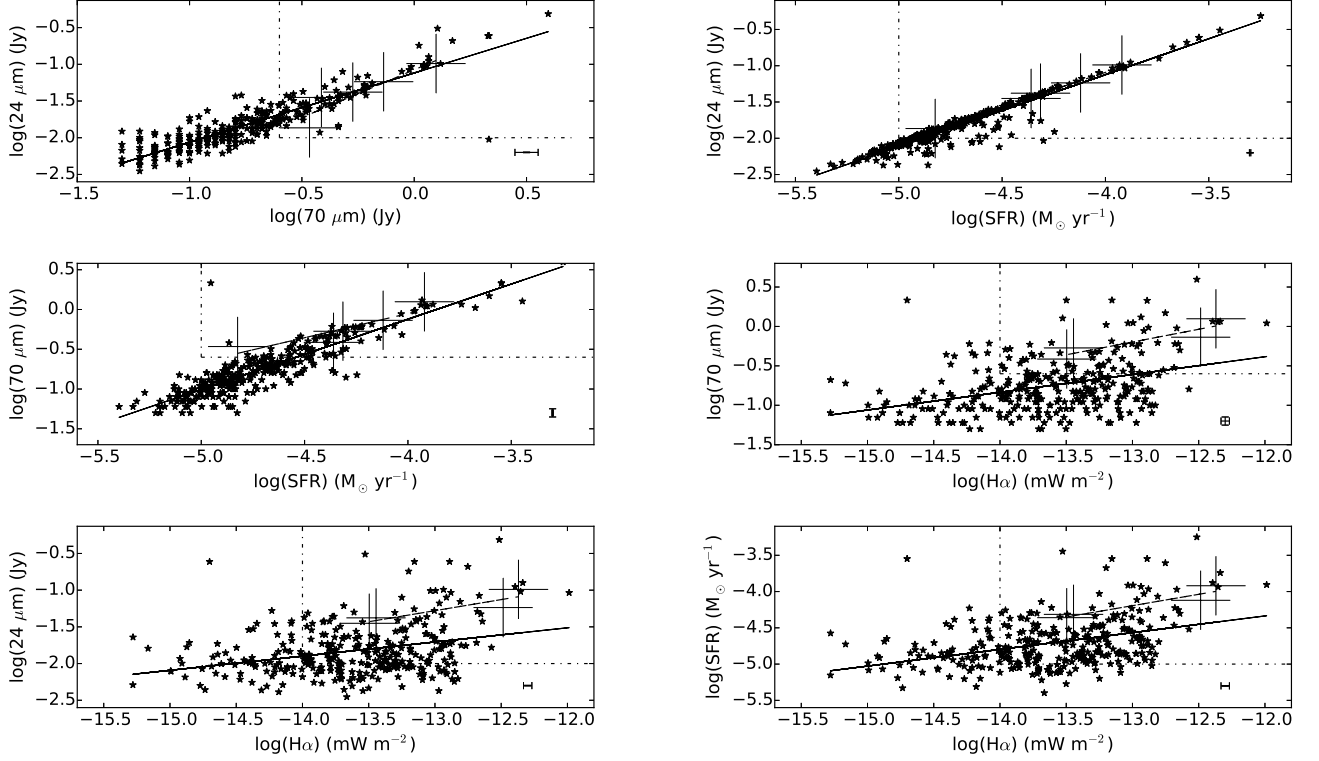


Figure 5. Relationships between the properties of the water maser and non-maser regions. Crosses indicate the water masers (enlarged for clarity), and stars indicate the non-masers. The dash-dotted lines show the regions of parameter space where water masers arise and where new water masers may be found (see text). Representative 1σ error bars are shown in the lower right of each panel.

Table 10. Pearson Correlation Coefficient p-values for the Non-Maser Sample

	T_{dust}	$\log(\text{SFR})$	$\log(24 \mu\text{m})$	$\log(70 \mu\text{m})$	$\log(160 \mu\text{m})$	$\log(\text{H}\alpha)$
T_{dust}		3.1×10^{-15}	6.4×10^{-12}	7.8×10^{-16}	5.7×10^{-3}	1.2×10^{-7}
$\log(\text{SFR})$			2.1×10^{-175}	3.0×10^{-113}	7.2×10^{-35}	9.7×10^{-13}
$\log(24 \mu\text{m})$				8.5×10^{-119}	9.4×10^{-39}	1.2×10^{-8}
$\log(70 \mu\text{m})$					7.8×10^{-47}	1.7×10^{-12}
$\log(160 \mu\text{m})$						1.9×10^{-4}
$\log(\text{H}\alpha)$						

regions selected from the Red MSX Survey (RMS), [Urquhart et al. \(2011\)](#) obtained an overall detection rate of $\sim 50\%$, but demonstrated a strong correlation between the H_2O maser detection rate and the bolometric luminosity. In order to compare this result to the M31 maser detection rate, we restrict the [Urquhart et al. \(2011\)](#) sample to the GBT luminosity sensitivity, $L_{\text{H}_2\text{O}} \geq 4.4 \times 10^{-4} L_{\odot}$, and re-calculate the detection statistics as a function of bolometric luminosity. Figure 8 shows this censored Galactic detection rate

that can be directly compared to the M31 detection rate.

Due to the small sample size and the fact that the detection rates for some luminosity bins correspond to zero or one, the standard binomial confidence interval that relies on the central limit theorem is not applicable. Instead we estimate the error bars using Wilson's score interval ([Wilson 1927](#)):

$$\frac{1}{1 + z^2/n} \left[\hat{p} + \frac{z^2}{2n} \pm z \sqrt{\frac{\hat{p}(1 - \hat{p})}{n} + \frac{z^2}{4n^2}} \right], \quad (2)$$

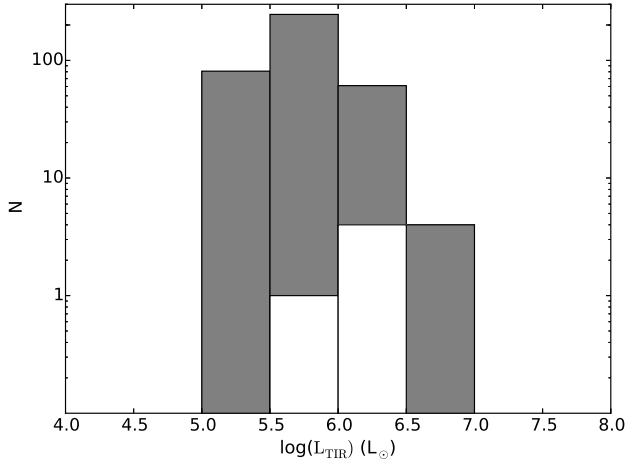


Figure 6. Distribution of the TIR luminosities of the M31 survey for the water masers (clear bins) and non-masers (shaded bins) listed in Tables 2 and 3.

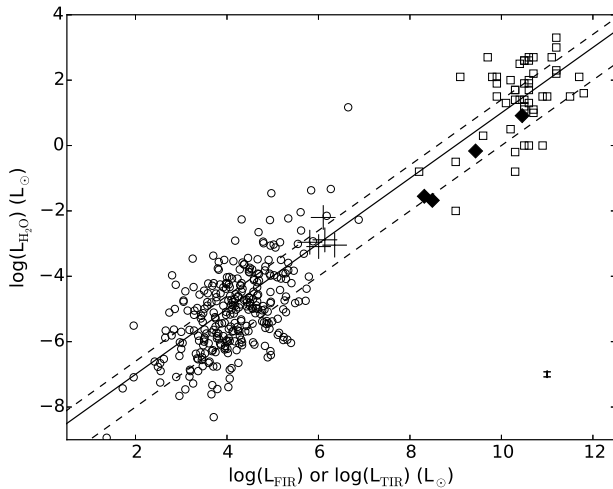


Figure 7. H_2O vs. FIR (or TIR) luminosity of Galactic and extragalactic water masers. The solid line shows the relation for Galactic star-forming regions (Jaffe et al. 1981), and the dashed lines show the relation for megamasers and kilomasers (Henkel et al. 2005; Castangia et al. 2008). Crosses mark the water masers in M31, the open squares indicate extragalactic H_2O megamasers and kilomasers obtained from Table 4 of Henkel et al. (2005) and references therein, filled diamonds indicate kilomasers associated with star formation in nearby galaxies (Darling et al. 2008), and open circles mark FIR luminosities and H_2O maser luminosities for Galactic water masers obtained from Urquhart et al. (2011). Representative error bars indicate 1σ uncertainties associated with the water masers in M31.

where z indicates the $1 - \alpha/2$ percentile of a standard normal distribution, \hat{p} is the estimated detection rate, and n is the number of samples. For a 95% confidence interval, $1 - \alpha/2 = 0.975$ and $z = 1.96$. An unconstrained least-squares fit to the non-zero data points for RMS

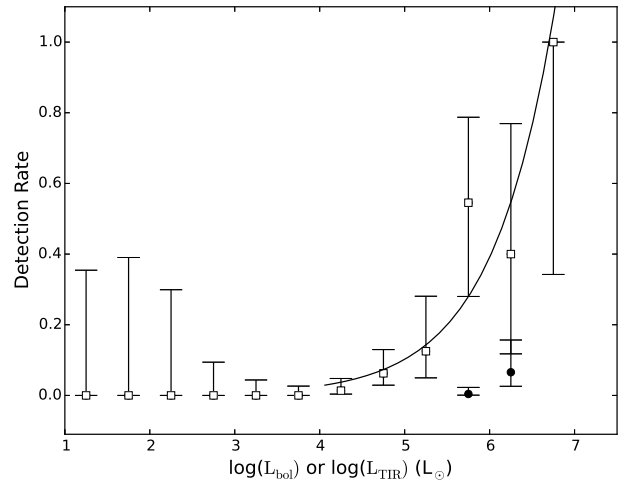


Figure 8. Water maser detection rate versus bolometric (or TIR) luminosity. Empty squares indicate the detection rate of the Galactic Urquhart et al. (2011) sample, adjusted to the luminosity sensitivity of the GBT M31 water maser survey ($4.4 \times 10^{-4} L_\odot$). Filled circles indicate the detection rate of the GBT M31 water maser survey. The solid line depicts a least-squares fit to the non-zero Urquhart et al. (2011) points. Error bars indicate the 95% confidence interval.

sources obtains the following relationship:

$$\log(\text{Detection Rate}) = (0.58 \pm 0.02) \times \log L_{bol} - (3.9 \pm 0.49), \quad (3)$$

which is plotted in Figure 8.

The filled circles in Figure 8 indicate the detection rate for the GBT M31 water maser survey. The detection rates in the two luminosity bins are $0.004^{+0.019}_{-0.003}$ ($5.5 < \log L_{TIR}/L_\odot < 6.0$) and $0.066^{+0.091}_{-0.040}$ ($6.0 < \log L_{TIR}/L_\odot < 6.5$). The upper and lower bounds indicate the 95% confidence interval. The water maser detection rates for the same luminosity bins in the censored Urquhart et al. (2011) sample are $0.55^{+0.24}_{-0.26}$ and $0.40^{+0.37}_{-0.28}$, respectively. The number of water masers in these luminosity bins is 11 and 5, whereas the number in the corresponding M31 bins is 1 and 4. Due to the small number of detected masers, these detection rates have large uncertainties, and the higher luminosity bin rates are statistically consistent between the two surveys (we omit from this statement the M31 bin that has a single maser). The M31 water maser detection rate thus does not significantly differ from the Galactic rate, although this is a statement more about poor statistics rather than about the nature of the masers in M31.

7. DISCUSSION

Water masers associated with star forming regions are known to trace shock regions in the outflows from both high mass and low mass young stellar objects (YSOs, Honma et al. 2005; Goddi et al. 2006; Moscadelli et al. 2006). VLBI observations often indicate water masers

trace disks and outflows (e.g. [Seth et al. 2002](#)). The most powerful masers in the Galaxy are associated with water masers in high-mass star-forming regions and flux densities of more than 10^4 Jy have been observed during maser flares (e.g., W49N) (e.g., [Liljestrom et al. 1989](#)). The water masers in M31, therefore, may show both offset velocities and significant variability, both of which may frustrate detection and proper motion studies.

7.1. Water Maser Surveys in the Galaxy

Water masers in the Galaxy have been observed toward ultra-compact HII (UCHII) regions and bright FIR sources. UCHII regions are small photoionized nebulae that are associated with earliest stages of massive star formation. [Churchwell et al. \(1990\)](#) surveyed a sample of bright IRAS FIR color-selected UCHII regions and detected water masers brighter than 0.4 Jy toward $\sim 67\%$ of the sources. Several other surveys have been performed toward known UCHII regions in the Galaxy. For example, [Palla et al. \(1991\)](#) obtained an overall detection rate of 17% using a 5 Jy detection limit (3σ), [Codella et al. \(1995\)](#) detected only 7% with a 6 Jy limit (3σ), and [Kurtz & Hofner \(2005\)](#) detected 55% using a 0.34 Jy sensitivity (3σ). The variable detection rates are due to selection criteria and sensitivity limitations (see [Kurtz & Hofner 2005](#), for a detailed discussion).

A catalog of 300 extended green objects (EGOs) were identified from the Spitzer Galactic Legacy Infrared Mid-Plane Survey Extraordinaire (GLIMPSE) project ([Cyganowski et al. 2008](#)). EGOs may represent massive young stellar objects still embedded in their infalling envelopes. They were identified based on their extended $4.5 \mu\text{m}$ (“green”) emission that likely traces shocked molecular gas from protostellar outflows. A survey of water masers in 94 northern EGOs showed a water maser detection rate of 68% for a median rms sensitivity of ~ 0.11 Jy ([Cyganowski et al. 2013](#)).

[Walsh et al. \(2011\)](#) performed a water maser survey of 100 deg^2 of the southern galactic plane using the Mopra Radio Telescope with rms noise of 1–2 Jy. They found 540 water masers, of which 340 are new detections. Based on the comparison of Galactic latitude distribution of the newly detected water masers with star-forming regions, they estimate at least 90% of the new detections originate in high-mass star-forming regions.

7.2. Evolutionary Stage of Water Masers

The evolutionary stage of water masers and which phase of massive star formation supports maser emission has been a topic of debate. Recently, [Sánchez-Monge et al. \(2013\)](#) studied the water maser and 22 GHz continuum emission of 194 southern massive star forming regions. They classified MYSOs based on the evolutionary scheme proposed by [Molinari et al.](#)

(2008) into three types, in order of increasing age:

- Type 1: Millimeter only sources. They are mainly high-mass protostars embedded in dusty clumps
- Type 2: Millimeter plus infrared sources. These objects are mainly zero age main sequence (ZAMS) OB stars with compact HII regions, but still embedded in dusty clumps.
- Type 3: Infrared-only sources. These objects are more evolved ZAMS OB stars surrounded by remnants of their parental clouds and contain extended and less dense HII regions.

Water masers were found to be mainly associated with Type 1 (13%) and Type 2 (26%) objects. Only 3% of Type 3 sources showed water masers. [Sánchez-Monge et al. \(2013\)](#) indicate that their results are consistent with evolutionary schemes (e.g., [Breen et al. 2010](#)) where water masers appear at the early stage of massive star formation, co-exist with HII regions and disappear while HII regions are still observable.

The bright $24 \mu\text{m}$ sources selected for the GBT M31 water maser survey belong to Type 2 and Type 3 classes. [Sánchez-Monge et al. \(2013\)](#) obtained an overall H_2O maser detection rate of 12% for Type 2 and Type 3 objects based on a single maser component sensitivity of ~ 2 Jy (5σ). Since 350 sources in the GBT survey are optically identified HII regions in the [Azimlu et al. \(2011\)](#) $\text{H}\alpha$ catalog, the GBT survey selection method may include many objects that are least likely to produce water masers (Type 3 objects). A more favorable means to detect water masers in M31 may be to select objects that show both mid-IR and mm continuum emission (Type 2 objects; see below).

Among the 457 non-maser sources, 346 objects have $\text{H}\alpha$ counterparts. The 111 objects with no $\text{H}\alpha$ identification either have low $\text{H}\alpha$ luminosity because they are in an early stage of star formation or they are highly obscured (or both). Among the five masers, one shows no $\text{H}\alpha$ emission, so the fraction of masers without $\text{H}\alpha$ emission is in agreement with the fraction among the non-masers: $20^{+22}_{-12}\%$ versus $24 \pm 2\%$, respectively.

To identify possible maser sites that may have been omitted from the GBT survey, we examined the $24 \mu\text{m}$ Spitzer map and the optically selected [Azimlu et al. \(2011\)](#) HII region catalog. We find at most 10 sources that show a strong correspondence between $\text{H}\alpha$ and $24 \mu\text{m}$ emission that had not been selected for the GBT water maser survey. Assuming the most optimistic maser detection rate of 26% (Type 2 objects) in the [Sánchez-Monge et al. \(2013\)](#) survey, and taking into account the poorer luminosity sensitivity of the GBT

survey, we would expect to find less than one additional maser in M31. This implies that we have likely detected the majority of water masers in M31 at the GBT survey sensitivity.

In order to increase the number of water masers detected in M31, one would like to perform water maser surveys of bright millimeter sources. The GBT surveys [Darling \(2011\)](#); [Darling et al. \(2016\)](#) targeted compact 24 μm sources in M31, which is associated with dusty molecular clouds and presumably star-forming regions. While this selection criterion includes a large fraction of active star forming regions in M31, it does not necessarily include all MYSOs embedded in dusty clumps that are only detectable at millimeter wavelengths (Type 1 objects) that show a 13% detection rate ([Sánchez-Monge et al. 2013](#)). Currently, there is no published millimeter continuum map of M31 available for a water maser survey focused on the earliest stages of star formation.

7.3. Comparison to Theory

High resolution observations of water masers in star-forming regions indicate that water masers are associated with shocks (e.g. [Goddi et al. 2011](#); [Moscadelli et al. 2011](#)). [Hollenbach et al. \(2013\)](#) present a theoretical model where water masers occur behind shocks with pre-shock densities in the range $\sim 10^6$ – 10^8 cm^{-3} . High velocity dissociative J shocks ($V_s \gtrsim 30 \text{ km s}^{-1}$) maintain a sufficient column of gas with temperatures (~ 300 – 400 K) heated by re-formation of H_2 to enable maser action. In this scenario a planar disk or slab with diameter 2ℓ (along the line of sight) and thickness d (perpendicular to the line of sight) maintains a large velocity coherent path length for maser action behind shock front. The aspect ratio of the maser geometry is defined as the ratio of the path length to the maser spot size: $a = 2\ell/d$. Using this model, [Hollenbach et al. \(2013\)](#) relate the observed maser parameters including the brightness temperature, luminosity, and maser spot size to the physical properties of the shock region.

For the five water maser complexes in M31, the size of maser spots and their brightness temperatures are unknown, and may remain unknown even with VLBI observations (the maser spot size is expected to be smaller than the best possible ground-based angular resolution). Also, observational determination of the shock velocity is not straightforward: proper motion measurements are required to determine the shock velocity of the gas, but this does not necessarily directly relate to the shock velocity ([Hollenbach et al. 2013](#)). The maser luminosities, however, can be measured and compared to theory.

The observed luminosities of individual maser lines in M31 ([Darling 2011](#)) can be used to investigate the properties of the shock regions. The luminosities of the

water masers in M31 are in the range $3.2 \times 10^{-4} L_\odot$ to $1.9 \times 10^{-3} L_\odot$. [Hollenbach et al. \(2013\)](#) show that the isotropic water maser luminosity of maser spots ranges from $3 \times 10^{-7} L_\odot$ to $10^{-5} L_\odot$ for aspect ratio $a = 10$ and pre-shock densities of $\sim 10^6$ – 10^8 cm^{-3} . Since luminosity scales with aspect ratio as a^3 , aspect ratios of ~ 30 – 180 are required to achieve the observed isotropic luminosities of water masers in M31. Similarly, [Hollenbach et al. \(2013\)](#) examine the brightest maser spot in W49N ($L_{iso} = 0.08 L_\odot$) and conclude that an aspect ratio of $a \geq 200$ is needed to produce the observed isotropic luminosity. Alternatively, high aspect ratios can arise from the alignment of two maser-producing regions ([Deguchi & Watson 1989](#); [Elitzur et al. 1991](#)). Clearly, the M31 water masers are exceptional, but they are consistent with the high-luminosity tail of the Galactic distribution.

The M31 water maser detection rate is 1.1(0.5)% ([Darling et al. 2016](#)). If all surveyed regions are producing masers, then the observed fraction C of maser-emitting regions indicates the maser emission angle: $C \sim \sin \theta_{em}$ ([Hollenbach et al. 2013](#)). Since it is more likely that only a fraction of the observed regions are producing masers, this becomes a lower bound on the maser emission angle: $\theta_{em} \simeq 1/(2a) \gtrsim 0.6^\circ$. This implies an aspect ratio $a \lesssim 45$, which is generally reasonable, but excludes the more extreme aspect ratios required by the high maser isotropic luminosities. The resolution of this tension likely lies in the fact that we are not detecting individual maser spots in M31, and therefore the isotropic luminosity of the maser spots is lower than we have inferred from single dish observations.

8. CONCLUSIONS

The multi-wavelength data used in this work enabled a comparative study of the properties of water maser-emitting regions and non-maser-emitting regions in M31. An enhanced network of water masers in M31 would enable precise proper motion and the proper rotation measurements of M31, but there do not seem to be many additional water masers to be found in the star-forming regions of the galaxy at the current survey sensitivity. We suggest three ways to detect additional water masers in M31:

1. Re-observe the most luminous mid- or far-IR sources with higher sensitivity than was used by the GBT. The known water masers in M31 represent the most luminous tail of the distribution, and improving a survey's sensitivity by a factor of a few should produce an order of magnitude more maser detections. The caveat with this approach is that these masers may not be bright enough for proper motion measurements using the sensitivity of current facilities.

2. Observe early-stage star-forming regions selected by mm continuum that have not been selected by their 24 μm emission. The detection rate among such a sample will be low, but the mm continuum selection offers a means to detect additional very luminous water masers that were missed in the GBT survey.

3. Re-observe the most luminous mid- or far-IR sources, and rely on maser variability for new detections. Masers are highly variable and short-lived, so among a sample of ~ 500 regions, newly luminous masers are a strong possibility over time baselines of 5–10 years.

In summary, this work demonstrated that:

- Water masers are associated with the highest star formation rate regions in M31, and a good detection strategy is to focus on the most luminous regions in any star formation proxy (mid- and far-IR or $\text{H}\alpha$ luminosity).
- The water masers in M31 are consistent with being analogs to water masers in Galactic star-forming regions and represent the high-luminosity tail of a larger (and as yet undetected) population. What is known about Galactic water masers can probably be applied to the water masers in M31.

The authors acknowledge support from the NSF grant AST-1109078. We are grateful to Matthew Smith and George Ford from the Herschel Exploitation of Local

Galaxy Andromeda (HELGA) team for providing access to Herschel SPIRE, dust temperature, and star formation rate maps of M31. We especially thank Bruno Altieri from European Space Agency (ESA) for re-processing the Herschel PACS map of M31. The authors thank K. Gordon for the Spitzer map and the anonymous referee for helpful comments. This research made use of NASA’s Astrophysics Data System Bibliographic Services, the NASA / IPAC Infrared Science Archive, and the NASA/IPAC Extragalactic Database (NED) and uses observations made with the *Spitzer Space Telescope*, all of which are operated by the Jet Propulsion Laboratory, California Institute of Technology, under a contract with NASA. This research made use of the observations made by the *Herschel Space Observatory*, an ESA space observatory with science instruments provided by European-led Principal Investigator consortia and with important participation from NASA. This publication makes use of data products from the Wide-field Infrared Survey Explorer, which is a joint project of the University of California, Los Angeles, and the Jet Propulsion Laboratory/California Institute of Technology, funded by the National Aeronautics and Space Administration. This research also made use of Montage, funded by NASA’s Earth Science Technology Office, Computational Technologies Project, under Cooperative Agreement Number NCC5-626 between NASA and the California Institute of Technology. The code is maintained by the NASA/IPAC Infrared Science Archive. Finally, this research made use of Astropy, a community-developed core Python package for Astronomy ([Astropy Collaboration et al. 2013](#)).

REFERENCES

- Astropy Collaboration, Robitaille, T. P., Tollerud, E. J., et al. 2013, *A&A*, 558, A33
- Azimlu, M., Marciniak, R., & Barmby, P. 2011, *AJ*, 142, 139
- Barmby, P., Ashby, M. L. N., Bianchi, L., et al. 2006, *ApJL*, 650, L45
- Breen, S. L., Caswell, J. L., Ellingsen, S. P., & Phillips, C. J. 2010, *MNRAS*, 406, 1487
- Brunthaler, A., Reid, M. J., Falcke, H., Greenhill, L. J., & Henkel, C. 2005, *Science*, 307, 1440
- Brunthaler, A., Reid, M. J., Falcke, H., Henkel, C., & Menten, K. M. 2007, *A&A*, 462, 101
- Calzetti, D., Kennicutt, Jr., R. C., Bianchi, L., et al. 2005, *ApJ*, 633, 871
- Castangia, P., Tarchi, A., Henkel, C., & Menten, K. M. 2008, *A&A*, 479, 111
- Churchwell, E., Walmsley, C. M., & Cesaroni, R. 1990, *A&AS*, 83, 119
- Codella, C., Palumbo, G. G. C., Pareschi, G., et al. 1995, *MNRAS*, 276, 57
- Cyganowski, C. J., Koda, J., Rosolowsky, E., et al. 2013, *ApJ*, 764, 61
- Cyganowski, C. J., Whitney, B. A., Holden, E., et al. 2008, *AJ*, 136, 2391
- Dale, D. A., & Helou, G. 2002, *ApJ*, 576, 159
- Darling, J. 2011, *ApJL*, 732, L2
- . 2013, *ApJL*, 777, L21
- Darling, J., Brogan, C., & Johnson, K. 2008, *ApJL*, 685, L39
- Darling, J., Gerard, B., Amiri, N., & Lawrence, K. 2016, *ApJ*, submitted
- Deguchi, S., & Watson, W. D. 1989, *ApJ*, 340, L17
- Elitzur, M. 1992, *ARA&A*, 30, 75
- Elitzur, M., McKee, C. F., & Hollenbach, D. J. 1991, *ApJ*, 367, 333
- Feigelson, E. D., & Babu, G. J. 2013, *Statistical Methods for Astronomy*, ed. T. D. Oswalt & H. E. Bond, 445
- Felli, M., Palagi, F., & Tofani, G. 1992, *A&A*, 255, 293
- Ford, G. P., Gear, W. K., Smith, M. W. L., et al. 2013, *ApJ*, 769, 55
- Goddi, C., Moscadelli, L., & Sanna, A. 2011, *A&A*, 535, L8
- Goddi, C., Moscadelli, L., Torrelles, J. M., Uscanga, L., & Cesaroni, R. 2006, *A&A*, 447, L9
- Gordon, K. D., Rieke, G. H., Engelbracht, C. W., et al. 2005, *PASP*, 117, 503
- Gordon, K. D., Bailin, J., Engelbracht, C. W., et al. 2006, *ApJL*, 638, L87

- Greenhill, L. J., Henkel, C., Becker, R., Wilson, T. L., & Wouterloot, J. G. A. 1995, *A&A*, 304, 21
- Groves, B., Krause, O., Sandstrom, K., et al. 2012, *MNRAS*, 426, 892
- Henkel, C., Peck, A. B., Tarchi, A., et al. 2005, *A&A*, 436, 75
- Hollenbach, D., Elitzur, M., & McKee, C. F. 2013, *ApJ*, 773, 70
- Honma, M., Bushimata, T., Choi, Y. K., et al. 2005, *PASJ*, 57, 595
- Humphreys, E. M. L., Reid, M. J., Moran, J. M., Greenhill, L. J., & Argon, A. L. 2013, *ApJ*, 775, 13
- Imai, H., Ishihara, Y., Kameya, O., & Nakai, N. 2001, *PASJ*, 53, 489
- Jaffe, D. T., Guesten, R., & Downes, D. 1981, *ApJ*, 250, 621
- Kurtz, S., & Hofner, P. 2005, *AJ*, 130, 711
- Laher, R. R., Gorjian, V., Rebull, L. M., et al. 2012, *PASP*, 124, 737
- Liljestrom, T., Mattila, K., Toriseva, M., & Anttila, R. 1989, *A&AS*, 79, 19
- Lo, K. Y. 2005, *ARA&A*, 43, 625
- Loeb, A., Reid, M. J., Brunthaler, A., & Falcke, H. 2005, *ApJ*, 633, 894
- Massey, P., Olsen, K. A. G., Hodge, P. W., et al. 2006, *AJ*, 131, 2478
- Merrett, H. R., Merrifield, M. R., Douglas, N. G., et al. 2006, *MNRAS*, 369, 120
- Molinari, S., Pezzuto, S., Cesaroni, R., et al. 2008, *A&A*, 481, 345
- Moscadelli, L., Cesaroni, R., Rioja, M. J., Dodson, R., & Reid, M. J. 2011, *A&A*, 526, A66
- Moscadelli, L., Testi, L., Furuya, R. S., et al. 2006, *A&A*, 446, 985
- Mould, J., Barmby, P., Gordon, K., et al. 2008, *ApJ*, 687, 230
- Nieten, C., Neininger, N., Guélin, M., et al. 2006, *A&A*, 453, 459
- Palla, F., Brand, J., Comoretto, G., Felli, M., & Cesaroni, R. 1991, *A&A*, 246, 249
- Piazzo, L. 2013, ArXiv e-prints, arXiv:1301.1246
- Pilbratt, G. L., Riedinger, J. R., Passvogel, T., et al. 2010, *A&A*, 518, L1
- Poglitsch, A., Waelkens, C., Geis, N., et al. 2010, *A&A*, 518, L2
- Reid, M. J. & Moran, J. M. 1981, *ARA&A*, 19, 231
- Reid, M. J. & Honma, M. 2014, *ARA&A*, 52, 339
- Sánchez-Monge, Á., Beltrán, M. T., Cesaroni, R., et al. 2013, *A&A*, 550, A21
- Seth, A. C., Greenhill, L. J., & Holder, B. P. 2002, *ApJ*, 581, 325
- Smith, M. W. L., Eales, S. A., Gomez, H. L., et al. 2012, *ApJ*, 756, 40
- Sohn, S. T., Anderson, J., & van der Marel, R. P. 2012, *ApJ*, 753, 7
- Sullivan, III, W. T. 1973, *ApJS*, 25, 393
- Urquhart, J. S., Morgan, L. K., Figura, C. C., et al. 2011, *MNRAS*, 418, 1689
- van der Marel, R. P., Fardal, M., Besla, G., et al. 2012, *ApJ*, 753, 8
- Walker, R. C., Matsakis, D. N., & Garcia-Barreto, J. A. 1982, *ApJ*, 255, 128
- Walsh, A. J., Breen, S. L., Britton, T., et al. 2011, *MNRAS*, 416, 1764
- Wilson, E. B. 1927, *Journal of the American Statistical Association*, 22, 158, 209
- Wright, E. L., Eisenhardt, P. R. M., Mainzer, A. K., et al. 2010, *AJ*, 140, 1868